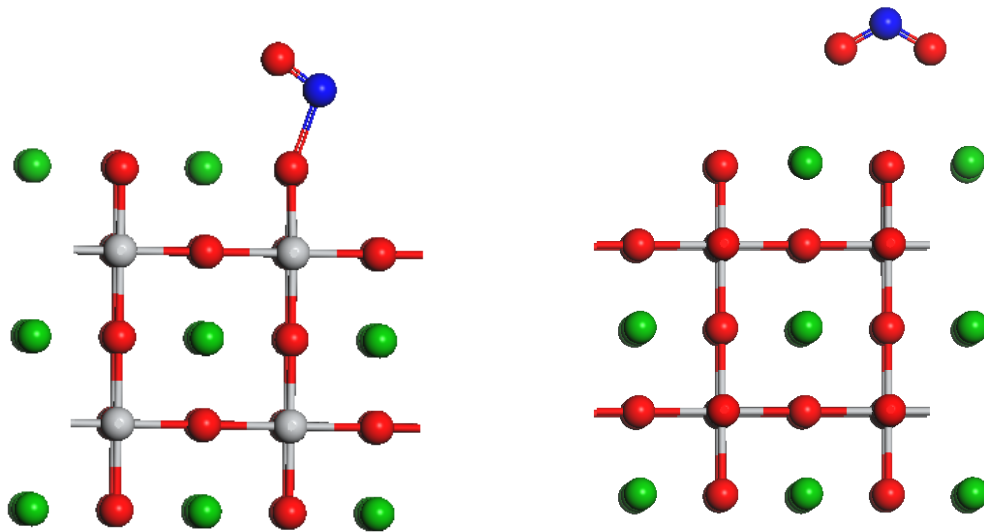


CHALMERS



First principle calculation of NO_x adsorption on ATiO₃ perovskites surfaces

BRITA ABRAHAMSSON

Department of Applied Physics
Division of Chemical Physics
CHALMERS UNIVERSITY OF TECHNOLOGY
Gothenburg, Sweden 2015
Master's Thesis 2014-2015

First principle calculation of NO_x
adsorption on ATiO_3 perovskites surfaces

BRITA ABRAHAMSSON

Department of Applied Physics
Division of Chemical Physics
CHALMERS UNIVERSITY OF TECHNOLOGY
Gothenburg, Sweden 2015
Master's Thesis 2014-2015

First principle calculation of NO_x adsorption on ATiO_3 perovskites surfaces
Brita Abrahamsson

©BRITA ABRAHAMSSON, 2015

Master's thesis report
Department of Applied Physics
Chalmers University of Technology
SE-412 96 Göteborg
Sweden
Telephone + 46 (0)31-772 1000

Printed at Chalmers Reproservice
Göteborg, Sweden 2015

Abstract

A promising solution to control NO_x -emissions in lean-burn engines is combined NO_x -trap and NH_3 -SCR catalysis, where NO_x is trapped in a storage material at low temperatures and then released and reduced by ammonia at temperatures around 150-200 °C. Here, adsorption of NO_x on perovskites with the structural formula ATiO_3 , A = Ca, Sr, Ba, have been studied within the Density Functional Theory, to investigate the compounds' capability of storing NO_x at desired temperatures. Comparisons are made with adsorption on alkali-earth metal oxide surfaces. DFT is employed with local basis functions using the PBE-functional and the perovskite-surfaces are modelled by the supercell periodic slab approach. The adsorption of NO is found to be a weak physisorption process, with desorption temperatures at around 250 K for AO-terminated Ba- and SrTiO₃. The interaction with NO₂ is stronger, and depends on the electropositivity of A (Ba>Sr>Ca). Dramatic cooperative effects are observed for pairwise adsorption of NO and NO₂. Negative charge is transferred from surface anion to NO₂ upon pair-adsorption, creating nitrite-like structures for both NO₂ and O-NO. The cooperative effect holds also for NO and O₂, with slightly lower adsorption energies.

Acknowledgements

First, I would like to thank my supervisor Henrik Grönbeck for being so enthusiastic about the project and for spending so much time discussing the project with me. I am also very grateful for the constructive feed back that he has given me.

Adriana, for the help and for all the good coffee-drinking and cake-eating times.

Julia, for being a great roommate!

Finally, I would like to thank each and everyone at Chemical Physics for their contribution to the nice atmosphere that surrounds the office.

Brita Abrahamsson, Gothenburg 01/2015

Contents

1	Introduction	1
1.1	Objectives	3
2	Theory	4
2.1	Quantum Chemistry	4
2.2	Density Functional Theory	5
2.2.1	The Thomas-Fermi approach	6
2.2.2	Hohenberg–Kohn Theorems	6
2.2.3	The Kohn-Sham Approach	7
2.2.4	Exchange-Correlation Functionals	8
2.3	DFT Implementation	9
2.3.1	Numerical Orbitals	10
2.3.2	Pseudo-potentials	11
2.3.3	Numerical Details	11
2.4	Calculated Experimental Observables	11
2.4.1	X-Ray Diffraction (XRD)	11
2.4.2	Temperature Programmed Desorption (TPD)	12
2.4.3	Infrared (IR) Spectroscopy	13
3	Bulk and Surface Properties	14
3.1	Bulk Structure of Perovskite Oxides	14
3.1.1	Properties of Cubic ATiO_3	15
3.1.2	Electronic Properties	16
3.1.3	Comparison to Alkali-Earth Metal Oxides	17
3.1.4	Structural distortions	17
3.2	Surface Modelling	18
3.2.1	Surface Terminations	20
3.2.2	Number of Layers	22
3.2.3	Supercell	22
3.2.4	Surface Energy	23

4	Adsorption	26
4.1	Adsorbates	26
4.2	Adsorption of NO and NO ₂ on ATiO ₃ -surfaces	27
4.3	Adsorption of NO and NO ₂ on AO-surfaces	28
4.4	Pairwise Adsorption of NO _x on ATiO ₃	30
4.5	Pairwise Adsorption of NO _x on AO	31
4.6	O ₂ Influence upon Adsorption	33
4.7	Electronic Structure Analysis	34
4.8	Calculated Experimental Observables	37
4.8.1	Temperature Programmed Desorption (TPD)	37
4.8.2	Vibrational Analysis	38
5	Discussion and Conclusions	41
	Bibliography	46

1

Introduction

The study of materials that can capture and reduce NO_x from engine exhaust gas is an important research field, as NO_x molecules have negative impact on the environment. N_2O is a greenhouse gas, much more potent than for example CO_2 and NO_2 is a toxic gas that contributes to acid rain.

The three way catalyst (TWC), used for conventional Otto-gasoline engines, is highly efficient in reducing NO_x compounds from the exhaust. However, diesel engines and engines that work at lean burn conditions (fuel burning with an excess of oxygen), have more efficient fuel use and lower carbon dioxide emissions compared to the conventional Otto engine [1]. Unfortunately, the NO_x reduction with TWC is not sufficient at lean conditions. Consequently, new methods have been developed, and two of the most promising solutions are the NO_x storage reduction (NSR, also known as the NO_x -trap) and the selective catalytic reduction of NO_x with NH_3 as a reducing agent (NH_3 -SCR) [2]. NSR-catalysis uses a storage material that adsorbs NO_x under lean conditions and then reduces the NO_x over a catalyst under short fuel rich periods [3], schematically depicted in Figure 1.1. In NH_3 -SCR, NO_x is instead reduced over a catalyst by a reducing agent, ammonia, provided from a solution of urea [1] as shown in Figure 1.2.

However, each of the methods have drawbacks. One problem with NSR is that other environmentally harmful compounds, such as ammonia, may be emitted in the exhaust [2]. Furthermore, the rich periods of operation results in a fuel penalty. In NH_3 -SCR, the catalyzed reduction of NO_x requires sufficiently high temperatures to work. For example, the dosage of urea requires temperatures higher than 200°C [1].

A possible solution to overcome the issue with low temperature activity for NH_3 -SCR is to use a passive NO_x -trap upstream the NH_3 -SCR catalysis. The idea is to use a storing material that adsorbs NO_x at low temperatures, preventing NO_x to escape during the time it takes for the engine to reach sufficient temperature, and then use the SCR-catalyst to convert this NO_x upon release at higher temperatures [4] as showed in Figure 1.3.

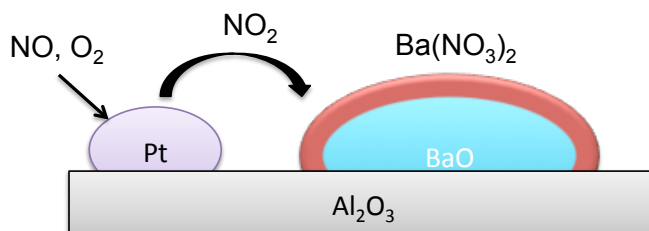


Figure 1.1: Schematic figure of a NO_x -trap.

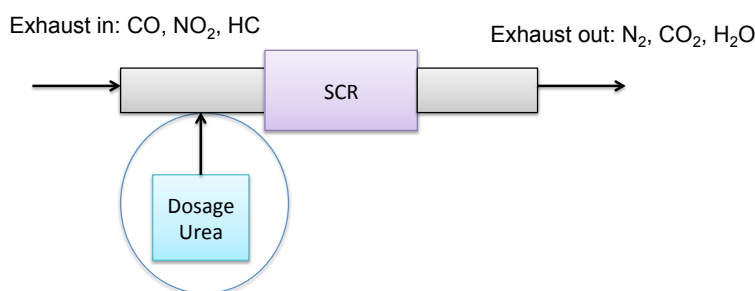


Figure 1.2: Schematic figure of NH_3 -SCR catalysis.

This brief introduction provides a motivation to study materials with tuned NO_x adsorption properties. Given that the NO_x storage properties of alkali-earth metal oxides have been explored in the past [5][3], it is interesting to consider other oxide materials, where metal oxides is one possibility. In this thesis, perovskites have been explored.

Mixed-metal oxides in the form of perovskite structure ABO_3 , have been under intense research during the past decades. A perovskite is a crystal structure rather than a specific material. The name originates from the first crystal with perovskite structure ever discovered, a calcium titanium oxide perovskite (CaTiO_3), which was first found in Siberia 1839 and named after mineralogist Lev Perovski. There are many different types of perovskites, some that exist abundantly in nature and others which are synthesized.

Most of the research on perovskite-materials in the early years focused on the materials' ferroelectric and magnetic properties. Years of research have shown that perovskite-like materials can adopt a variety of interesting physical properties. IBM's Zurich Research Laboratory used SrTiO_3 as model structure when investigating insulating oxides and later it was discovered that the properties of the crystal could be changed by al-

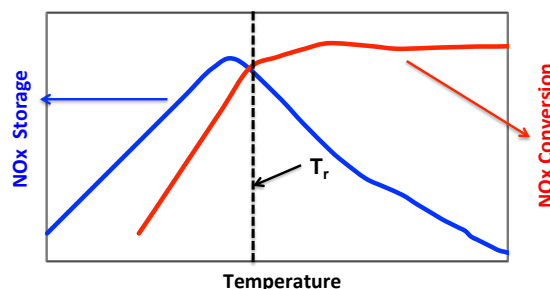


Figure 1.3: Schematic figure of the capability of a NO_x trap storing NO_x generated at $T < T_r$ (blue) and the catalytic conversion of NO_x at $T > T_r$ (red).

tering the composition of the material. Most interestingly, the material could turn into a superconductor by removing oxygen from some lattice positions [6]. Perovskites have also been explored as catalytic materials, where the work on CO-oxidation is one early example [7].

Here, the interaction between NO_x on ATiO_3 -surfaces will be studied, with $A = \text{Ba}$, Sr and Ca . By altering the A-ion, the adsorption energy can be changed, which gives the possibility to tune the desorption temperature.

1.1 Objectives

The objective of the study is to investigate the potential of perovskite oxides as storing material in the combined NO_x -trap/ NH_3 -SCR catalysis. This will be studied by *ab initio* calculations within the Density Functional Theory (DFT). Geometrical and electronic structure analysis will be performed on the surface both with and without adsorbates in order to gain understanding about what mechanisms are involved in the adsorption process. Moreover, the results are compared with calculations of NO_x adsorption on alkali-earth metal oxides, which are currently in use in the industry. Future comparisons with experimental results are made possible by calculations of TPD and IR-spectra.

2

Theory

Computational chemistry is a scientific field that has been under rapid development during the past decades. One can explain this by the great advances in computational efficiency, which enable calculations for systems with increasing complexity. Properties that are difficult, dangerous or costly to measure experimentally can instead be calculated through simulations [8, p.12]. Moreover, theory can predict properties of systems and explain experimental results, why experimentalists and theoreticians currently lives in mutual symbiosis with each other.

2.1 Quantum Chemistry

A key concept in quantum mechanics is the particle-wave duality. Quantum mechanics was developed when it became clear that microscopic particles not only behave as particles, described by classical mechanics, but also have wave-like properties. As classical mechanics was unable to describe this duality of the system accurately, quantum mechanics was developed in the 1920s [9].

A state of a system is described by a wave function. The wave function itself is not an observable, but by applying operators corresponding to physical observables one can obtain expectation values for all physical properties of interest [8, p. 106]. The goal of most quantum mechanical methods is to find an approximate solution to the Schrödinger equation (the ultimate goal is to solve for it exactly!) [10, p. 3]. The Schrödinger equation reads:

$$H\Psi = E\Psi \tag{2.1}$$

Here, H is the Hamiltonian, which is the operator for the total energy of the system, Ψ is the wave function of the system and E is a number representing the energy of the state described by Ψ .

For a system of N electrons and M nuclei, the Hamiltonian takes the form (expressed in atomic units)¹ [8, p. 107]:

$$H = -\frac{1}{2} \sum_{i=1}^N \nabla_i^2 - \frac{1}{2} \sum_{A=1}^M \frac{1}{M_A} \nabla_A^2 - \sum_{i=1}^N \sum_{A=1}^M \frac{Z_A}{r_{iA}} + \sum_{i=1}^N \sum_{j>i}^N \frac{1}{r_{ij}} + \sum_{A=1}^M \sum_{B>A}^M \frac{Z_A Z_B}{R_{AB}} \quad (2.2)$$

where the terms (going from left to right) represent the kinetic energy of the electrons, the kinetic energy of the nuclei, the potential energy between nuclei and electrons, the potential energy between electrons and the potential energy between nuclei.

There are only a few systems for which there exists an analytic solution to the Schrödinger equation; why a lot of researchers have spent a lot of time finding approximations to simplify it. The first step is generally the Born-Oppenheimer approximation (BOA), which assumes that nuclei are stationary particles. This approximation is motivated by the fact that a nucleus has much greater mass than an electron, which has the consequence of the nucleus moving much slower [8, p. 110]. The BOA simplifies the Hamiltonian to the so called electronic Hamiltonian, which reads (also in atomic units) [10, p. 5]:

$$H_{el} = -\frac{1}{2} \sum_{i=1}^N \nabla_i^2 - \sum_{i=1}^N \sum_{A=1}^M \frac{Z_A}{r_{iA}} + \sum_{i=1}^N \sum_{j>i}^N \frac{1}{r_{ij}} = T + V_{Ne} + V_{ee} \quad (2.3)$$

The subscript *el* will be dropped as the electronic Hamiltonian will be used throughout the thesis.

The energy of a system can be obtained from taking the expectation value of the Hamiltonian [11, p. 108]:

$$E = \frac{\langle \Psi | H | \Psi \rangle}{\langle \Psi | \Psi \rangle} \quad (2.4)$$

As the wave function is such a problematic quantity (it is not an observable and it depends on $4N$ variables [10, pp. 29]), there has been a search for other, simpler, quantities that can fully describe a many-body system. One candidate is the electron density, which is a quantity that only depends on three variables, the three Cartesian coordinates.

2.2 Density Functional Theory

This section will give a brief description of the fundamental ideas behind the density functional theory (DFT), and shortly mention the most ground-breaking steps that have made it possible for DFT to become the important tool that it is today, not only in computational chemistry, but also in material science, a field which has had an explosion

¹The atomic unit (au) system is defined by setting the mass of an electron, the charge of an electron, the reduced Plancks constant ($\hbar/2\pi$) and the permittivity of vacuum to unity, $m_e = e = \hbar = 4\pi\epsilon_0 = 1$. These values define the system, and other related physical constants are derived from them [10].

of DFT-related articles during the past years [12]. It begins with the first successful formulation of a DFT-energy expression ever made, and continues with contributions from Hohenberg-Kohn [13] and Kohn-Sham [14].

2.2.1 The Thomas-Fermi approach

The first successful attempt to describe a many-body system's total energy as a functional of the electron density was made independently by Thomas and Fermi in 1927 [15]. The electrons in the system were considered as a non-interacting uniform gas, creating a system with constant electron density. This approximation resulted in a very simple expression for the kinetic energy of the system [8, p. 251]:

$$T[\rho(r)] = \frac{3}{10}(3\pi^2)^{2/3} \int \rho^{5/3}(r)dr \quad (2.5)$$

The rest of the energy contributions, the electron-nuclear and electron-electron interaction were treated in a classical way, which lead to the following expression of the total energy of the system [10, p. 31]:

$$E_{TF}[\rho(r)] = \frac{3}{10}(3\pi^2)^{2/3} \int \rho^{5/3}(r)dr - Z \int \frac{\rho(r)}{r}dr + \frac{1}{2} \int \int \frac{\rho(r_1)\rho(r_2)}{r_{12}}dr_1dr_2 \quad (2.6)$$

The sum of the energy contributions was minimized subject to the constraints [10, p. 31]:

$$\rho(r) > 0, \int \rho(r)dr = N \quad (2.7)$$

Thomas and Fermi managed to describe the energy of the system completely in terms of electron density, which is an important step in the DFT-history. Unfortunately, the obtained energies were not accurate enough to properly describe the chemical properties of real systems [15].

2.2.2 Hohenberg-Kohn Theorems

The first of the two very important DFT-contributions that Hohenberg-Kohn made, was to prove that the electron density *uniquely* determines the external potential, which means that the total energy is a unique functional² of the ground-state density [13]. The total energy with all its contributions is written [10, p. 34]:

$$E[\rho] = \int \rho(r)V_{Ne}dr + T[\rho] + E_{ee}[\rho] \quad (2.8)$$

The terms in equation 2.8 can be divided into two parts, the universally valid system independent contributions $T[\rho]$ and $E_{ee}[\rho]$ and the system dependent term $\int \rho(r)V_{Ne}dr$,

²A functional is a function that uses a vector as input argument (oppose to a function which takes a scalar as input) and returns a scalar as output.

where V_{Ne} is the external potential. The electron-electron interaction term can be further divided into the classical Coulomb-interaction $J[\rho]$ and the non-classical exchange-correlation interaction E_{xc} , which gives the expression:

$$E[\rho] = \int \rho(r)V_{Ne}dr + T[\rho] + J[\rho] + E_{xc}[\rho] \quad (2.9)$$

The second important contribution that Hohenberg–Kohn made [13] was to show that the energy of a system has a global minimum when the electron density variable takes the value of the ground state density, or in other words, that the ground state density determines the ground state energy.

2.2.3 The Kohn-Sham Approach

Kohn and Sham made the next ground-breaking step in DFT [15]. Thomas and Fermi’s attempt was not accurate enough and Kohn and Sham realized that the main flaw of their energy expression was to be found in the crude approximation of the kinetic energy. Kohn-Sham solved this by introducing an imaginary system of non-interacting electrons, moving in an effective potential v_{eff} . The effective potential should be assigned the value that gives the non-interacting and the interacting system (the system under consideration) the same electron density.

The electron density is given by:

$$\rho(\mathbf{r}) = \sum_i |\varphi_i(\mathbf{r})|^2 \quad (2.10)$$

where φ_i are the so called Kohn-Sham orbitals (KS-orbitals), which should satisfy the one-electron eigenvalue function [10, p. 43]:

$$h^{KS}\varphi_i(\mathbf{r}) = \epsilon_i\varphi_i(\mathbf{r}) \quad (2.11)$$

where h^{KS} is the one-electron operator defined as [10, p. 43]:

$$h^{KS} = -\frac{1}{2}\nabla^2 + v_{eff} \quad (2.12)$$

Once the KS-orbitals are known, the kinetic energy of the non-interacting system can be solved *exactly* [10, p. 44]:

$$T_s = -\frac{1}{2}\sum_i^N \langle \varphi_i(\mathbf{r}) | \nabla^2 | \varphi_i(\mathbf{r}) \rangle \quad (2.13)$$

This is really the genius of Kohn-Sham’s approach. As the kinetic energy is a major part of the total energy of the system, it is important to get a good approximation of this term (recall the H-atom where the kinetic energy is 13.6 eV, which is half of the absolute value of the potential energy). By introducing a non-interacting system with orbitals, one can obtain the exact kinetic energy of this system. The only unknown energy

contribution in equation 2.9 is the exchange-correlation functional (E_{xc}), which does not only include non-classical exchange-correlation effects but in principle also corrections for the self-interaction (electrons should not interact with themselves!) and the remainder of the kinetic energy that is not covered by the kinetic energy of the non-interacting system. To be expressed mathematically [10, p. 44]:

$$E[\rho]_{xc} = (T[\rho] - T_s[\rho]) + (E_{ee}[\rho] - J[\rho]) \quad (2.14)$$

Kohn-Sham's approach of replacing a complicated problem with a less complicated one, transforms the many-body interaction problems into an independent particle problem with all tricky non-classical interaction terms in an exchange-correlation functional.

The anchor between the imaginary non-interacting system and the real, interacting system, is the effective potential. In order for the electron density of the two systems to become equal, v_{eff} needs to equal the sum of the potential the electrons experience from the nuclei (v_{Ne}), the Coulomb potential (v_{ee}) and the exchange-correlation potential (v_{xc}) generated by E_{xc} .

$$v_{eff} = v_{Ne} + v_{ee} + v_{xc} \quad (2.15)$$

Since v_{xc} is unknown, approximations need to be introduced in this step in order to get v_{eff} , which is needed to obtain the KS-orbitals, which in turn are needed to obtain the ground-state density and, furthermore, the ground-state energy. Due to this self-entanglement in the solution chain, the problem has to be solved iteratively; a matter which will be discussed in Section 2.3.

2.2.4 Exchange-Correlation Functionals

The exchange correlation energy (corresponding to v_{xc}) can, at least in principle, be solved exactly for small systems. However, this is more expensive than solving the Schrödinger equation directly, why all practical uses of DFT involves approximations for it [12]. There have been many different proposals for approximating exchange-correlation functionals, a few of which will be mentioned below.

Local density approximation

One of the results from the Kohn-Sham approach, where the kinetic energy from the non-interacting system and the long ranged Hartree-potential (Coulomb-interaction) are separated from the other contributions, is that the remaining exchange-correlation functional can be considered a rather local functional of the density [16, p 153]. This is the idea behind the local density approximation (LDA) where the exchange-correlation density in each point is approximated as that of a homogenous gas with that density [10, p 71].

$$E_{xc}^{LDA} = \int \rho(\mathbf{r}) \epsilon_{xc}(\rho(\mathbf{r})) d\mathbf{r} \quad (2.16)$$

This approximation is best suited for solids where the exchange and correlation interaction effects are short ranged. However, for inhomogeneous systems, LDA is a rather poor approximation [16, p. 152-153]. The performance of LDA for perovskites is shown in Section 3.1.

Generalized Gradient Approximation

Even though the LDA performs well enough to be used for material research in solid-state physics, it is not accurate enough to determine many chemical properties (for example, bond energies are typically overestimated by 1 eV/bond [15]). One way to improve the approximation is to expand the exchange correlation functional to include information about the gradients of the charge density [10, 76]:

$$E_{xc}^{GGA} = \int \rho(\mathbf{r}) \epsilon_{xc}(\rho, \nabla \rho) d\mathbf{r} \quad (2.17)$$

2.3 DFT Implementation

One common KS-DFT application is to expand the KS-orbitals φ_i , in a Linear Combination of Atomic Orbital (LCAO). The idea is to linearly combine determined basis functions, χ_i , to expand φ_i .

$$\varphi_i(\mathbf{r}) = \sum_{i=1} c_{ij} \chi_i \quad (2.18)$$

By using predefined basis functions, the only unknowns are the expansion coefficients c_i . As the name suggests, the approach was first used with hydrogen-like orbitals (s, p, d...) as basis functions. Nowadays, the basis functions don't necessary resemble atomic orbitals very much. Instead, it is of great importance to choose functions that are easy to compute and that gives fair approximations of the molecular orbitals when linearly combined. The before-mentioned eigenvalue equation reads:

$$h^{KS} \varphi_i(\mathbf{r}) = \epsilon_i \varphi_i(\mathbf{r}) \quad (2.19)$$

Inserting the expanded expression for φ_i and the one-electron energy operator h^{KS} in Equation 2.4, the expectation value of the energy reads [8, p 113]:

$$E = \frac{\int \left(\sum_i c_i \varphi_i \right) h^{KS} \left(\sum_j c_j \varphi_j \right) d(\mathbf{r})}{\int \left(\sum_i c_i \varphi_i \right) \left(\sum_j c_j \varphi_j \right) d(\mathbf{r})} \quad (2.20)$$

This expression can be rearranged to form [8, p 114]:

$$E = \frac{\sum_{ij} c_i c_j H_{ij}}{\sum_{ij} c_i c_j S_{ij}} \quad (2.21)$$

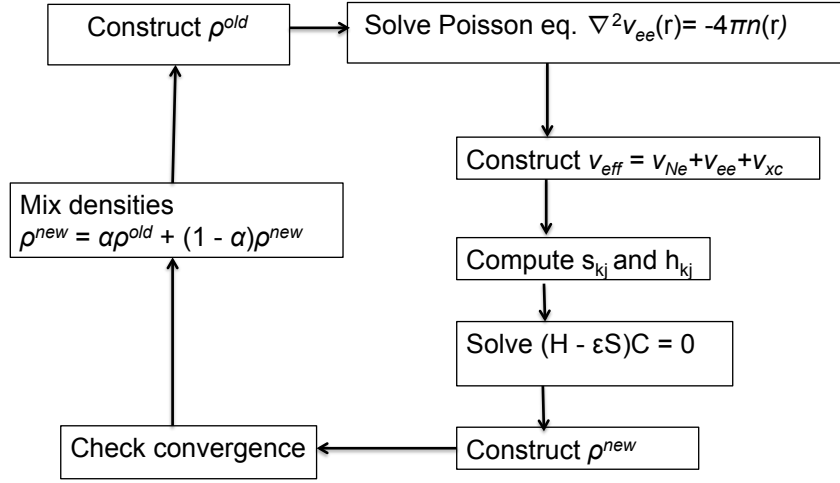


Figure 2.1: A schematic figure describing the iterative process of the self-consistent loop.

The energy expression is minimised with respect to the expansion coefficients, to obtain the KS-orbitals that corresponds to the lowest energy of the system [8, p 114]:

$$\frac{\delta E}{\delta c_k} = 0 \quad (2.22)$$

Equation 2.21 leads to N equations (known as the secular equations), which must be satisfied in order for Equation 2.22 to hold [8, p 114]:

$$\sum_{i=1}^N c_i (H_{ki} - ES_{ki}) = 0 \quad (2.23)$$

The eigenvalue equation is now transformed from a non-linear problem to a linear matrix equation, which can efficiently be solved by computer algorithms. As h^{KS} depends on the electron density, the density is needed to solve the secular equation which generates the KS-orbitals. However, the electron density is calculated from the KS-orbitals; why the solution is dependent on the solution so to speak. Because of this, the Kohn-Sham scheme has to be solved iteratively, by a so called self-consistent loop, schematically depicted in Figure 2.1. The numerical procedure to solve the Poisson equation generating v_{ee} and the integration is described in [17].

2.3.1 Numerical Orbitals

This project implements the Kohn-Sham DFT in the program Dmol, which uses numerical orbitals as basis functions χ_i . Numerical functions generate very compact basis sets, which means that the computational cost can be kept low [18]. There are three alternatives for numerical basis sets in Dmol; dn, dnd and dnp, which differ in size (number of functions used to span the molecular orbitals). The d in the basis sets denote double numerical basis; which means that all occupied outer shell orbitals are described by two

basis functions. The smallest set of the three, dn, uses two basis functions per orbital. The basis set is significantly improved when polarization functions are added, which are functions with a higher angular momentum than the momentum of the highest occupied orbital in the atom [17]. For instance, if the bonding to an He-atom should be modelled, not only the two numerical functions describing the 1s-orbital ($l=0$) would be included in the basis set, but also functions to describe the higher angular momentum 2p-orbital ($l=1$). The only difference between dnd and dnp is that dnd does not include polarization functions for hydrogen atoms (but do so for all other atom types).

2.3.2 Pseudo-potentials

Valence electrons play the lead role in chemical bonding, why it seems reasonable to distinguish between valence and core electrons. One way to keep the computational cost low is to simply eliminate the core electrons from the calculation, and replace their charge by an effective potential that the valence electrons experience (effective core potential). A less simplified version is to fix the core electrons so that they remain unaffected by electron density redistributions caused by chemical bonding formation [18]. A frozen core approximation saves a lot of computational time and should not lower the accuracy in a significant way [17].

2.3.3 Numerical Details

For the remainder of the project, the DFT is employed with local basis functions using the PBE-functional, which is a type of GGA-functional developed by Perdew, Burke and Ernzerhof (explained in depth in [19]). If nothing else's stated, the dnp-base set will be used. Semi-core pseudo potentials are used and the global cut-off radius is 6.1 Å for all calculations. The k-point sampling for slab-calculations will be $3 \times 3 \times 1$ and for bulk-calculations $6 \times 6 \times 1$.

2.4 Calculated Experimental Observables

Results obtained from DFT-calculations should not be trusted blindly and comparisons with experiments are of great importance for verification. For this cause, experimental observables are calculated to enable comparisons between obtained results and experiments. The experimental methods which are used for comparison are briefly described in this section.

2.4.1 X-Ray Diffraction (XRD)

XRD is an important experimental technique for structure analysis of compounds. The popular powder diffraction technique is able to generate a fingerprint of the structure of a material [20, p 212]. XRD is based on the phenomenon of diffraction, which is the kind of wave interference that occurs when an object is in the path of the waves. For diffraction to arise, the wavelength of the beam has to be in the same size range as

the spacings in the object that's in the way. The interlayer spacing between atoms in materials are in the size range of Ångström (10^{-10} m), why X-ray is a good choice of radiation to obtain diffraction patterns from layers of atoms [20, p 212]. In the powder diffraction technique, a beam of X-ray is shot on to a powder sample. The diffraction intensity is measured by a detector, which is moved so that the beam hits the sample from different angles. The results of the XRD is analyzed by the Bragg equation:

$$2d\sin\theta = \lambda \quad (2.24)$$

Here, d is the spacing between the atom layers, related to the angle θ at which interference occur [20, p 212]. XRD can be used to identify a solid material by comparing the intensities and angles with reference samples from a data base. XRD is also used to measure the size of a material's unit cell [9, p 260].

2.4.2 Temperature Programmed Desorption (TPD)

Temperature Programmed Desorption (TPD) is a method for estimating bond energies between adsorbates and surfaces. A surface with adsorbed molecules is heated (normally with a specified rate, the so called β -rate), until the energy transferred from the surface to the adsorbate is high enough for the molecule to desorb from the surface [9, p 708]. Naturally, the desorption temperature increases with the strength of the interaction.

A theoretical TPD-spectra can be approximated by the Arrhenius-like Polanyi-Wigner equation, where the coverage with respect to time is expressed as follows [21]:

$$-\frac{d\theta}{dt} = A\theta^n \exp\left(\frac{-E_d(\theta)}{RT}\right) \quad (2.25)$$

Here, A is the pre-exponential factor, θ is the coverage, n is the kinetic order of the reaction, R is the gas constant and E_d is the activation energy of desorption. In principle, A and E_d depends on the coverage. By letting the temperature increase linearly, one can through the β -rate convert the expression from being a function of time to a function of temperature [21].

$$T(t) = T_0 + \frac{dT}{dt}t = T_0 + \beta t \quad (2.26)$$

$$\frac{d\theta}{dT} = A\frac{\theta^n}{\beta} \exp\left(\frac{-E_d}{RT}\right) \quad (2.27)$$

Here, $\frac{d\theta}{dT}$ is the so called coverage intensity. By plotting the coverage intensity with respect to temperature, peaks in the plot will reveal the desorption temperatures. This theoretical description of the coverage intensity excludes entropy effects. Also, it does not include the possibility of readsorption, which is a fair assumption for adsorption experiments performed in Ultra High Vacuum (UHV).

2.4.3 Infrared (IR) Spectroscopy

The characteristic vibrational frequencies of a molecule depend on two things; the masses of the molecule's atoms and the stiffness of the bond between the atoms. The number of ways a molecule can vibrate depends on its size (number of atoms) and structure. A polyatomic ($N \geq 3$), linear molecule has $3N-5$ vibrational modes and a non-linear molecule has $3N-6$ modes [22, p.23]. The vibrations can be divided into two different groups; stretching and bending modes, where the bending mode generally corresponds to lower vibrational energies (lower frequencies), as the potential energy is changed more rapidly with bond stretching than with angle [9, p 322]. NO_2 which consist of three atoms, have three vibrational modes ($3*3-6$); two stretching (symmetric and antisymmetric) and one bending. Dimers, such as NO and O_2 , only have one stretching mode.

The vibrational frequencies of a molecule are within the range of infrared (IR) radiation, which means that molecules can become vibrationally excited when hit by photons [20, p 92]. This is used in IR-spectroscopy, where the frequencies at which a molecule adsorbs radiation generates a characteristic pattern that can be compared with reference data to identify the molecular species. Furthermore, as proper reference data is missing for many systems, comparisons to calculations are also used for interpretation of measurements.

3

Bulk and Surface Properties

Adsorption occurs on the surface of a material, why proper surface modelling is an important step when simulating the adsorption process. This chapter begins with a brief description of the perovskite-oxide structure and criteria that must be fulfilled for compounds to form perovskite structure. It continues with mentioning a few bulk properties of interest, where the lattice parameter is the most important one for the subsequent surface modelling. In order to check stability and rigidity of the bulk material, a brief discussion about the formation energy and bulk modulus for the different perovskite-oxides is included. Furthermore, the computed bulk structures are compared with experimental results from XRD-analysis. The chapter continues with the surface modelling, where a periodic surface is created with the optimised bulk units as building blocks.

3.1 Bulk Structure of Perovskite Oxides

A mineral with perovskite-oxide structure has the chemical formula ABO_3 , where A is a relatively large and B is a relatively small cation. The A-ion is placed in each corner of the cell, the B-ion in the centre and the anions (oxygen) are face-centered positioned, illustrated in figure 3.1. The perovskites in this study have the formula $ATiO_3$, where $A = Ba^{+2}$, Sr^{+2} or Ca^{+2} .

There are two main criteria that must be fulfilled in order for the perovskite structure to be stable. The first one is electroneutrality. The sum of the oxidation numbers of the ions must equal zero.

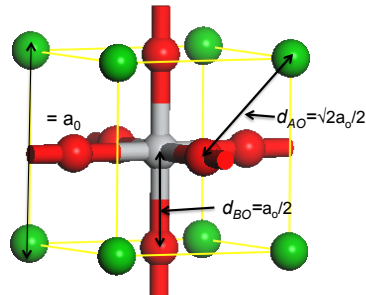


Figure 3.1: The structure of a cubic perovskite unit cell with A-ion (green), Ti (grey) and O (red).

Table 3.1: Calculated lattice parameters (a_0) using two different E_{xc} , bulk modulus (B), t-values and formation energies (E_f) the considered perovskites. Experimental values for lattice parameters (Exp), literature values for bulk modulus (Lit) and A-ion radii (r_A) are also included. Lattice parameters and ion-radii are given in Å, formation energy in eV.

A-ion	a_0			r_A Exp	t	B		E_f GGA
	GGA	LDA	Exp [25]			GGA	Lit [26]	
Ca	3.88	3.81	3.84	1.14	0.85	196.6	192.4	-0.62
Sr	3.94	3.86	3.91	1.32	0.91	176.3	181	-1.27
Ba	4.04	3.95	4.01	1.49	0.97	144.9	165	-1.39

The second critical factor are absolute and relative values of the atomic radii. The lower limit for the A-ion radius (r_A) for a perovskite oxide is 0.51 Å and the relative sizes between the ion radius must be such that the tolerance factor t stays within the range $0.75 < t < 1$, where t is defined as [7]:

$$t = \frac{(r_A + r_O)}{\sqrt{2}(r_B + r_O)} \quad (3.1)$$

The relevant distances are indicated in Figure 3.1.

3.1.1 Properties of Cubic ATiO₃

The lattice parameter is the length of the bulk unit cell, as shown in Figure 3.1. Starting with an initial guess $a = b = c = a_o$ for a cubic perovskite, the bulk unit is geometrically optimised to obtain the most energetically favourable structure, generating the optimised values of a_0 , presented in Table 3.1. Not surprisingly, the lattice parameter increase with increased A-ion size. The lattice parameters are calculated with two different choices of E_{xc} . A comparison with experiments suggests that the GGA-functional gives too long lattice constants whereas the lattice constants calculated with LDA are too short. These are known functional artifacts that have been reported in previous publications for metal-oxide materials [23]. However, the deviations from experimental values can be considered rather low.

The formation energy of a perovskite is another interesting property, since it is closely connected to the chemical and thermal stability of the material [24]. A more negative formation energy suggests a more stable structure and positive formation energy indicates that the compound is not formed spontaneously. The formation energy for ATiO₃ is calculated by:

$$E_f = E(ATiO_3) - E(AO) - E(TiO_2) \quad (3.2)$$

From the formation energies in Table 3.1, it is clear that CaTiO₃ has a lower (less negative) formation energy than the perovskites with larger lattice constants, indicating that the cubic CaTiO₃ is a less stable compound than the cubic Sr- and BaTiO₃.

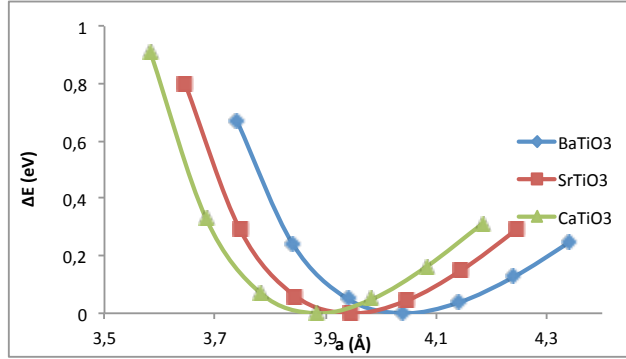


Figure 3.2: The energy penalty is plotted against the lattice parameter. The reference energy ($E=0$) represents the energy corresponding to the optimised $l a_0$.

The bulk modulus is a measure of the rigidity of a material. Table 3.1 indicate that the bulk modulus decrease with an increased lattice parameter. This agrees well with previous studies suggesting that the bulk modulus is linealy dependent on the lattice parameter for cubic $A^{+2}B^{+4}O_3$ -perovskites [26]. The rigidity increase when the material can be packed more closely, *i.e.* when the lattice parameter is small. The more rigid the material, the higher the energetic penatly when altering the lattice parameter from its optimal value, as shown in Figure 3.2.

3.1.2 Electronic Properties

The Density of States (DOS), is a very useful tool for illustrating the electronic properties of a system. The DOS depicts the number of states that electrons can occupy at a given interval of energy, defined by:

$$DOS(E)dE = \# \text{levels between } E \text{ and } E+dE$$

When integrating the DOS up to the Fermi level (dashed line in Figure 3.3), the total amount of occupied states in the system is obtained [27]. A projected DOS (PDOS), projects the total DOS on the available states of selected atoms in order to see the character of the states. Figure 3.3 shows the projected density of states on to the 2p-oxygen (red) and 3d-titane orbitals (blue). The valence band is of O-character whereas the conduction band is mainly Ti. The DOS includes a lot of information such as HOMO and LUMO-levels and also reveals the band gap (energy difference between HOMO and LUMO) of the

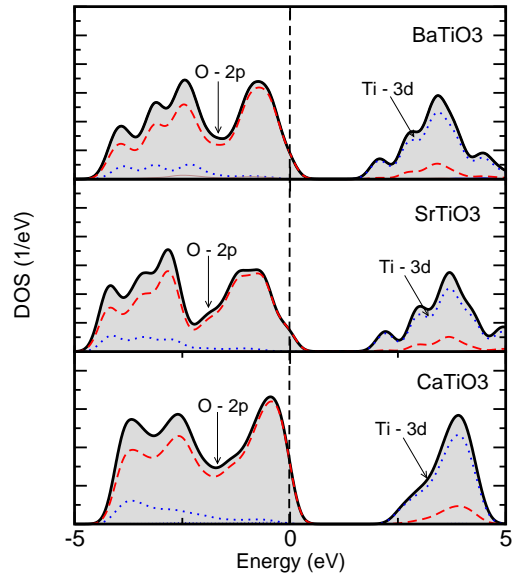


Figure 3.3: The DOS for the different cubic perovskite-oxide bulks.

system, which seem to increase with decreased A-ion size (Ca>Sr>Ba). Studies made on alkali-earth metal oxides (AO) suggest that the observed band dispersion is a result of different oxygen nearest neighbor overlap [23]. The oxygen atoms in AO:s with small A-ions are more closely packed, which creates an increased energy difference between the HOMO and LUMO-orbitals, an explanation that holds for perovskite-oxides as well.

3.1.3 Comparison to Alkali-Earth Metal Oxides

It is interesting to compare the NO_x adsorption on perovskite surfaces with alkali-earth metal oxides. Bulk optimization calculations are performed in the same manner as described in previous sections, but for AO:s instead of ATiO_3 . GGA-calculations on optimized AO-bulk units give lattice parameters 4.83, 5.22 and 5.63 Å for CaO, SrO and BaO, respectively. Calculated values agrees well with experiments (4.81, 5.16 and 5.54 Å [28]). Previous theoretical studies on AO-bulk and experimental findings show that CaO is the most stable alkali-earth metal oxide and that the bulk modulus increase with decreased A-ion size [23].

3.1.4 Structural distortions

The ideal cubic perovskite structure is rarely encountered as it requires high temperatures and t-values close to 1 [7, pp 241]. Figure 3.1 shows that for a bulk unit to be cubic, d_{AO}/d_{BO} should equal $\sqrt{2}$, which generates a t-value of one. All three studied perovskite-oxides are within the range of forming perovskite structure (t-value between 0.75 and 1). However, only Ba and Sr have t-values close enough to unity to be expected to form cubic structure, which demands a t-value between 0.9 and 1 [7, p 241]. The low formation energy of CaTiO_3 is another sign that indicates that it is not stable in its cubic structure. Furthermore, my initial calculations of NO and NO_2 adsorption on surfaces made up from cubic CaTiO_3 -units shows peculiar behaviour. The calculated adsorption energies for NO_x -molecules on cubic CaTiO_3 -slabs are unphysically high and it is apparent from structure analysis that a lot of the energy originates from structural relaxations in the perovskites rather than from the adsorption process itself. All of these things indicate that the CaTiO_3 bulk unit is *not* stable in its cubic structure.

In order to confirm this hypothesis, X-Ray Diffractions constructed from the optimised cubic structures in Table 3.1, are compared with XRD:s from Chalmers synthesized Ba, Sr and CaTiO_3 -perovskites [N.Wilken and M.Skoglund (unpublished)]. From Figure 3.5, it is apparent that the experimental and theoretical XRD:s for Ba- and SrTiO_3 resemble each other, suggesting that their bulk structures are, indeed, cubic. However, a comparison between XRD:s from synthesized CaTiO_3 and optimised cubic structure does not agree as well with each other, shown in Figure 3.6. The reason for the instability of the cubic CaTiO_3 can be realized by the following argument. The building blocks when forming ATiO_3 are two metal-oxides, one AO-unit and one TiO_2 -unit. It is clear from Figure 3.4 that the A-O distance is about the same in the metal-oxide as in the cubic perovskite for the Ba-case.

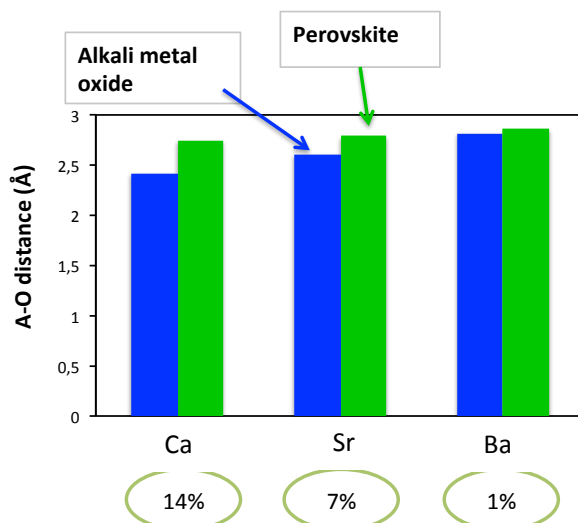


Figure 3.4: AO-distances (Å) in the metal oxides (blue) and perovskites (green) and the demanded elongation of the AO-distance when going from oxide to perovskite.

However, for the Ca-case, the A-O distance has to be elongated with about 14 % when going from CaO to cubic CaTiO₃-structure. This increased distance between the atoms is not reasonable and yields structural distortions. Orthorhombic distortions are common for perovskites with tolerance factors in the range 0.75 – 0.90, where CaTiO₃ is found according to Table 3.1.

Literature suggests a distorted structure for CaTiO₃ with lattice parameters $a=5.38$, $b=5.44$ and $c=7.64$ Å [29]. The optimised lattice parameters of the suggested structure, calculated with GGA, are $a=5.41$, $b=5.51$ and $c=7.70$ Å and the calculated formation energy of the bulk is -0.93 eV. The XRD from the optimised distorted structure shows considerably better agreement with the experimental XRD than the cubic structure does (Figure 3.6), concluding that CaTiO₃ is distorted from its ideal cubic structure. The final bulk unit structures in Figure 3.12 shows that the distorted bulk cell consists of four units, which are tilted to fit the distances between the atoms.

3.2 Surface Modelling

Adsorption occurs on the surface of a material, which makes proper surface modelling an important step when investigating the process of adsorption. There are two conceptual ways of modelling a surface, the cluster and the periodic slab approach [18]. In this study, a periodic slab has been used to model the surface, why an in-depth description of the cluster approach is beyond the scope of this thesis.

The surface is created by the cleavage of bulk material. The perovskites in this project are cleaved in the (0 0 1) direction, which means that the z-axis is in the direction normal to the surface. The bulk units, optimised as described in the previous section, are cleaved

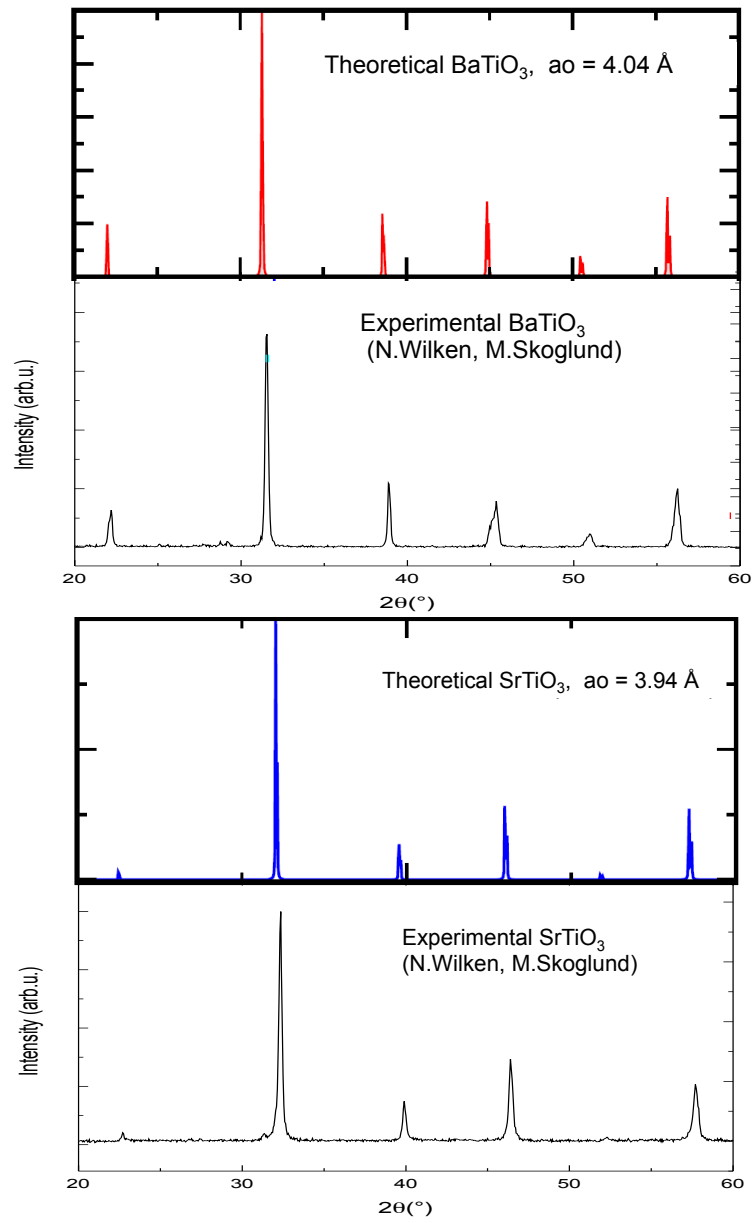


Figure 3.5: XRD from experimental BaTiO₃ and SrTiO₃ compared with XRD from optimised structures.

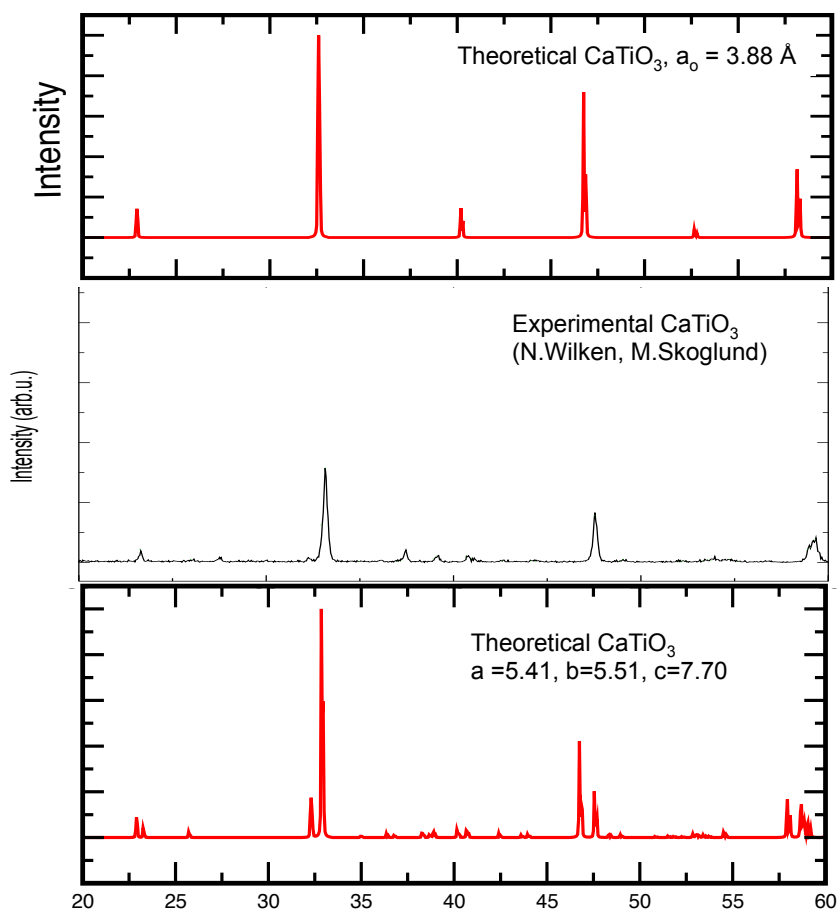


Figure 3.6: XRD from optimised distorted structure (top), experimental (middle) and optimised cubic structure (bottom) of CaTiO_3 .

to form a surface which is modelled by a periodic slab, depicted in Figure 3.8.

The bulk units are endlessly repeated in 2D (x and y), creating an infinite surface. The slab thickness (number of bulk units repeated in the z -direction) should be enough for surface properties to remain unchanged upon a further addition of layers.

3.2.1 Surface Terminations

There are three different possible surface terminations when creating the periodic slab. Either, the slab is asymmetric with one TiO_2 -terminated and one AO -terminated surface, as in Figure 3.9 a. Or, the slab is symmetric, meaning that the two surfaces are terminated with the same metal-oxide, either AO - or TiO_2 (Figure b and c in 3.9).

At a first glance, it might be tempting to choose an asymmetric slab, as it is stoichiometric (each slab consists of an integer number of bulk units). However, the disadvantage of having an asymmetric slab is that a dipole moment is created perpendicular to the

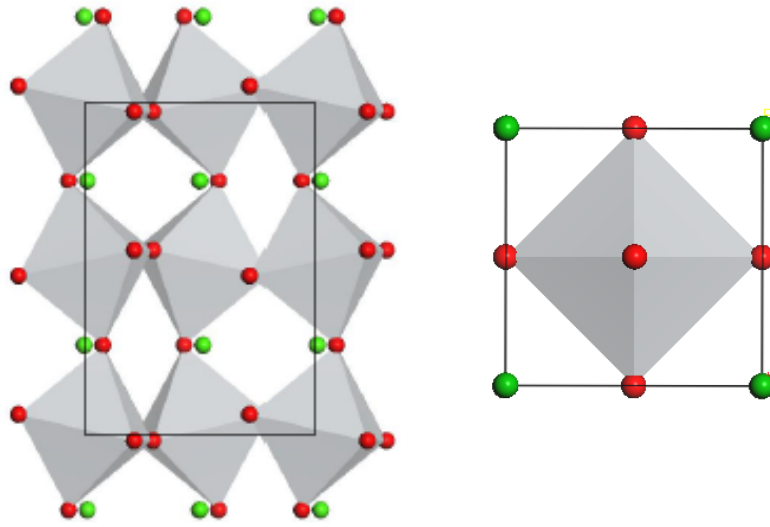


Figure 3.7: The polyhedron bulk structure of the distorted CaTiO_3 (left) and the cubic BaTiO_3 (right).

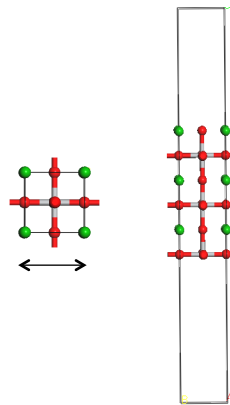


Figure 3.8: An optimised bulk unit and a periodic 6-layer slab

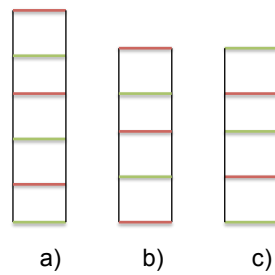


Figure 3.9: A schematic figure of a 6-layer asymmetric, 5-layer AO- and TiO_2 -terminated 1×1 -slab (going from left to right).

Table 3.2: Interlayer distance between Ti and O (d), distance (perpendicular to the surface) between O and Ti or Ba (dz) and a measure of the surface energy (E_s) for an *asymmetric* slab with varying amount of layers. Distances are given in Å and E_s in J/m².

Layers	$d(\text{O-Ti})$	$dz(\text{Ba-O})(\text{Å})$	$d(\text{Ti-O})$	$dz(\text{Ti-O})$	E_s (J/m ²)
4	1.89	0.06	1.87	0.11	1.86
6	1.90	0.05	1.88	0.11	1.89
8	1.90	0.04	1.88	0.12	1.88
10	1.90	0.04	1.87	0.12	1.86

slab surface. This is a result of the difference in covalency between the A-O and the Ti-O bond, where the former is much more ionic than the latter, which makes the AO- and TiO₂-layers differently charged. A redistribution of electronic charge is induced in order to eliminate this dipole moment, which can have an impact on the optimised coordinates of the atoms [30]. In order to eliminate the risk of this effect, a symmetric slab is chosen in this study.

3.2.2 Number of Layers

The slab thickness should be enough for the surface properties to converge with respect to the number of layers. This has been investigated by relaxing the entire slab, with a varying number of layers, and then calculate surface properties. The surface properties studied in order to determine the number of layers needed, are the interlayer distance between atoms in top and second layer, relative displacement of atoms in the top layer and a measure of the surface energy.

It seems as the investigated properties remain fairly constant for $N > 5$ (recall that a symmetric slab gives an uneven number of layers), why the number of layers are set to five. Of course, an increase of layers result in more computationally demanding calculations, why there is a reason to keep the number of layers as low as possible. To further decrease the computational time and to prevent relaxation energies to be a too large contribution to the adsorption energy, 3 out of 5 layers are fixed, which means that the Cartesian coordinates of the atoms in these layers are fixated [23].

3.2.3 Supercell

To be able to investigate adsorption processes with low coverage, the repeated unit cells have to be sufficiently large [18]. Therefore, a supercell periodic slab is created, where each repeated unit has the dimension 2x2x1 (each repeated unit consists of four bulk units). Two periodic slabs are seen from above in Figure 3.10. An NO-molecule is adsorbed on to the slabs to illustrate the different sizes of the repeated units. However, since the CaTiO₃-unit cell is larger than the unit cell of Ba and Sr, there is no need for

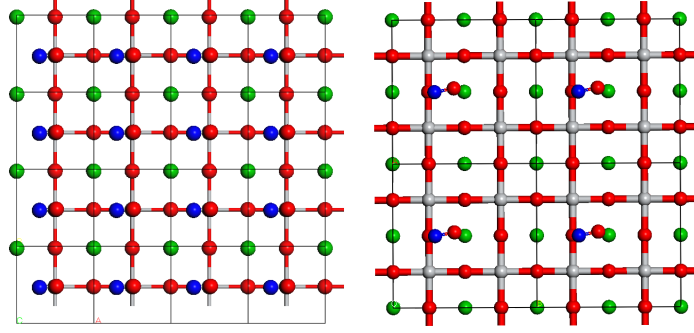


Figure 3.10: NO adsorbed on 1x1-slab (left) and on 2x2-slab (right) seen from above.

using a (2x2) supercell for the Ca-case.

3.2.4 Surface Energy

As previously mentioned, a symmetric slab is chosen in order to avoid the creation of a dipole-moment. There are two possible surface terminations of the symmetric slab, the AO- and the TiO_2 -termination. To investigate which one of the terminations are more likely to exist experimentally, the surface energy of the two surfaces are calculated.

Calculating the surface energy of a symmetric slab is not trivial. When calculating the surface energy for an asymmetric slab, one simply subtracts the energy for one bulk unit times the number of units from the total energy of the slab. However, this results in a surface energy where the contributions from the two terminations are mixed. A symmetric slab on the other hand, is not created by an integer number of bulk units, why it is a bit trickier to calculate its surface energy. There are several ways to calculate the surface energy of a symmetric slab [31]. Heifets *et al.* pointed out that the surface energy is the sum of two energy contributions: the cleavage and the relaxation energy. The two differently terminated five-layer slabs consist of five bulk units in total where the AO-terminated slab consist of three AO-layers and two TiO_2 -layers and the TiO_2 terminated slab of three TiO_2 -layers and two AO-layers. When cleaving a bulk unit, the two different surfaces are created simultaneously, why it seems fair to assume that the cleavage energy is the same for both terminations. The cleavage energy is calculated:

$$E_c = \frac{1}{4} [E_{slab}^{(unrel)}(AO) + E_{slab}^{(unrel)}(\text{TiO}_2) - NE_{bulk}] \quad (3.3)$$

where $E_{slab}^{(unrel)}(AO)$ and $E_{slab}^{(unrel)}(\text{TiO}_2)$ are the total energies of the unrelaxed AO- and TiO_2 -terminated slabs, respectively. The relaxation energy is then calculated in a fairly intuitive manner:

$$E_r(X) = \frac{1}{2} [E_{slab}(X) - E_{slab}^{(unrel)}(X)] \quad (3.4)$$

where X represents AO or TiO_2 . The total surface energy is then the sum of the two

Table 3.3: The surface energy (σ) of the three perovskites, calculated as a sum of the relaxation energy (E_r) and the cleavage energy (E_c) divided by the area. E_r and E_c are given in eV, the area in \AA^2 and σ in $\text{eV}/\text{\AA}^2$.

Type	$E_r(\text{AO})$	$E_r(\text{TiO}_2)$	E_c	Area	$\sigma(\text{AO})$	$\sigma(\text{TiO}_2)$
CaTiO_3	-0.31	-0.22	2.89	30.16	0.085	0.089
SrTiO_3	-0.37	-0.52	5.11	62.26	0.076	0.073
BaTiO_3	-0.16	-0.35	4.46	65.29	0.066	0.063

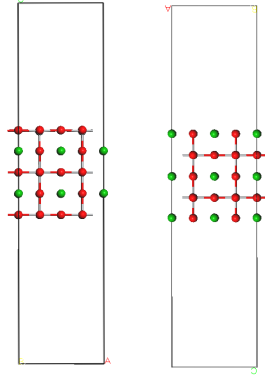


Figure 3.11: Symmetric, 5-layer periodic supercell slabs, TiO_2 - (left) and BaO -terminated (right).

contributions:

$$\sigma(X) = E_c + E_r(X) \quad (3.5)$$

[32]

According to the calculations (Table 3.3), the most stable surface for Ba and Sr is the TiO_2 -terminated one, whereas the most stable one for Ca is the CaO -terminated surface. However, the differences in surface energy is low and one can expect that both terminations are formed experimentally.

The surface model that will be used for the adsorption simulations are periodic 2×2 , 5-layer slabs where 3 of the layers are fixed for Ba and Sr, depicted in Figure 3.11, and a 1×1 slab for Ca depicted in Figure 3.12. The slabs are cleaved from optimised bulk units which are fixed under slab relaxation.

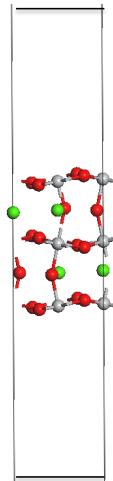


Figure 3.12: Distorted CaTiO₃-slab (TiO₂-term).

4

Adsorption

There are two types of adsorption processes; physisorption and chemisorption. Physisorption is the weaker of the two and the main force in this process is Van der Waals-forces. The electronic structure of the adsorbate and surface remains, relatively, unaffected by the process. Chemisorption, on the other hand, involves a chemical reaction between surface and adsorbate, resulting in an altered electronic density distribution. The mechanism that occurs when molecules are chemisorbed onto a metal oxide surface is normally considered to be either an acid/base or redox-reaction between the surface and adsorbate [5].

This chapter will begin with a brief description of the molecules that will be used as adsorbates, presenting calculated gas phase properties and electron level diagrams. It continues with NO and NO₂ adsorption on ATiO₃-surfaces and by pair-adsorption, where two NO_x molecules are adsorbed simultaneously. NO_x adsorption have been performed on both terminations for all perovskite-types. The results for the adsorption on the perovskite surfaces are compared to NO_x adsorption on alkali-earth metal oxide surfaces.

To avoid repetitions for the reader, most analysis regarding electronic structure redistributions and calculations of experimental observables have been focused on one system; the BaO-terminated BaTiO₃-perovskite. The choice of system can be motivated by the fact that the barium oxide (BaO) has renowned capacity of storing NO_x (used in NSR-catalysis), why the BaO-terminated perovskite can be anticipated to interact with NO_x.

4.1 Adsorbates

This project deals with three adsorbates; NO, NO₂ and O₂. In order to identify structural and electronic changes of the adsorbate when exposed to a surface, it is important to calculate their gas-phase properties. Calculations on simple and well-known systems are also valuable as a measure of the accuracy of the DFT-approximation, through com-

Table 4.1: Calculated and experimental bond lengths and vibrational energies for NO [33, p 475], NO₂ [34] and O₂ [33, p 497], using two different basis sets. Vibration energies are given in cm⁻¹ and bond lengths in Å.

Adsorbate	Basis	Bond Length	Vibrational Energy		
NO	dn	1.20	1649		
	dnp	1.16	1893		
	Exp	1.15	1904		
NO ₂	dn	1.26	663	1148	1356
	dnp	1.19	741	1338	1641
	Exp	1.21	750	1318	1641
O ₂	dn	1.29	1308		
	dnp	1.23	1547		
	Exp	1.21	1580		

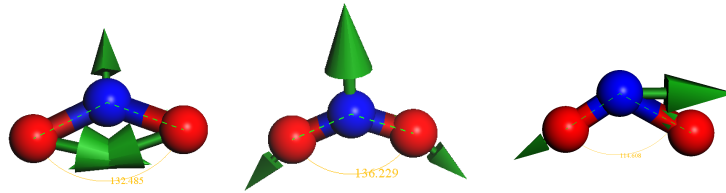


Figure 4.1: Vibrational modes for NO₂: bending $E_{vib}=741$ (left), symmetric $E_{vib}=1338$ (middle) and antisymmetric stretching $E_{vib}=1641$ (right).

parisons with experimental values. The gas phase properties are presented in Table 4.1, calculated with two different basis sets. As expected, calculations performed with the larger basis set dnp, which includes polarization functions, agrees better with experimental values. The three different vibrational modes of NO₂, presented in Table 4.1, are depicted in Figure 4.1.

The frontier orbitals of the adsorbates are important for the interaction with the surface. In Figure 4.2, energy diagrams for a part of the valence are shown for NO, O₂ and NO₂.

4.2 Adsorption of NO and NO₂ on ATiO₃-surfaces

NO and NO₂ are adsorbed separately on to both terminations on all perovskite-types. Numerous simulations with different initial positions of the adsorbate on to the surface, shows that NO-adsorption with N down is stronger compared to O down, where N binds

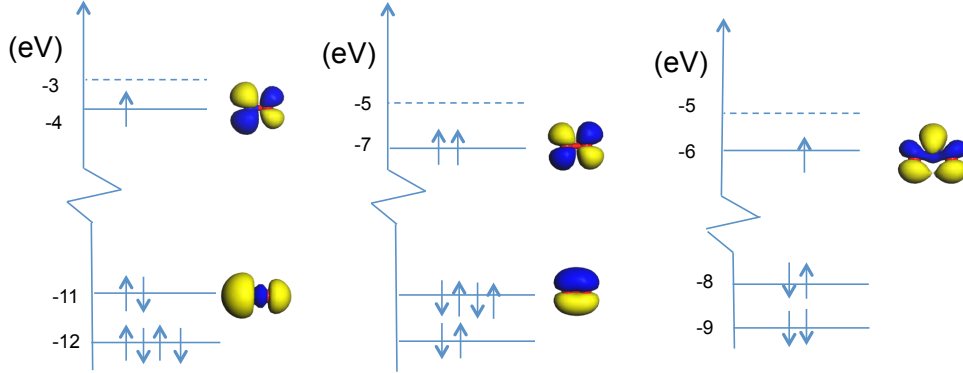


Figure 4.2: The orbital energy level diagram for NO (left), O₂ (middle) and NO₂ (right). The dashed line represents the LUMO-level.

to either surface O²⁻, or in some cases, surface Ti⁴⁺. The most favorable adsorption structure for NO₂ is when NO₂ is bridged between two A-ions or two Ti-ions, depicted in Figure 4.3. The adsorption energies, presented in Table 4.2, are calculated by:

$$E_{ads}(NO_x) = E(tot) - E(slab) - E(NO_x)_g \quad (4.1)$$

Here, E(tot) is the total energy of the system (slab + adsorbate), E(slab) is the energy of a bare slab and E(NO_x)_g is the total energy of gas-phase NO_x. All of the systems are relaxed.

The interaction between adsorbate and ATiO₃-surface increase with the decrease in electronegativity of the A-ion, according to the sequence Ba > Sr > Ca. The trend is obvious for NO₂-adsorption, as shown in Figure 4.4, which agrees well with previous studies indicating that the NO₂ interaction with ATiO₃ is related to the electropositivity of the alkali-earth metal (Ba > Sr > Ca) [35]. However, the trend does not seem to hold for NO-adsorption on AO-terminated surfaces, where Figure 4.4 show that the adsorption energy remain constant for all perovskites. Adsorption is generally stronger on AO-terminated surface, with the exception of NO-adsorption on BaTiO₃, where the adsorption energy is higher for the TiO₂-terminated surface.

4.3 Adsorption of NO and NO₂ on AO-surfaces

Results from calculations of NO_x-adsorption on alkali-earth metal oxide surfaces are shown in Table 4.3. NO is adsorbed with N down on to surface O²⁻. The adsorption energy increases with the electropositivity of the A-ion (Ba > Sr > Ca) for both NO and NO₂. Moreover, the interaction energies are stronger than for the perovskite surfaces.

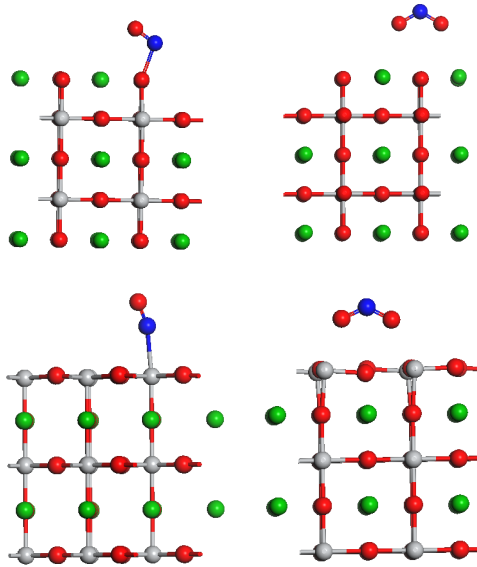


Figure 4.3: Adsorption of NO (left) and NO₂ (right) on to BaO-(top) and TiO₂-terminated (bottom) BaTiO₃-surfaces.

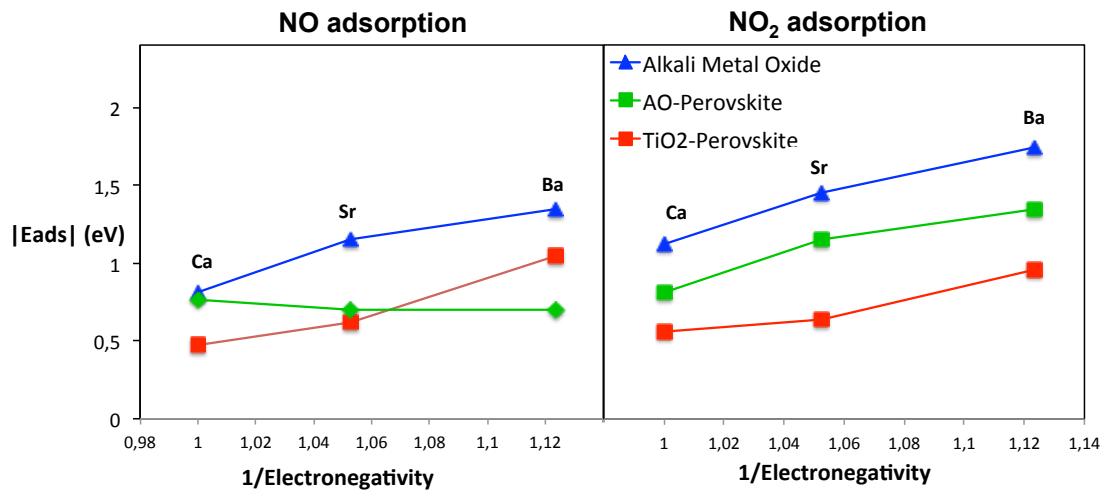


Figure 4.4: Adsorption energies for NO (left) and NO₂ (right) on AO- and TiO₂-terminated perovskites and alkali-earth metal oxides, plotted against the inverse electronegativity.

Table 4.2: Adsorption energies and angles between NO and surface O (O-NO) and NO₂. Distances between NO and surface O (O/Ti-NO) for isolated adsorbed NO_x on two different terminations of ATiO₃. Adsorption energies are given in eV and distances in Å.

Type	Term	O-NO (°)	O/Ti-NO (Å)	NO ₂ (°)	E _{ads} (NO)	E _{ads} (NO ₂)
CaTiO ₃	AO	109.0	2.00	123.5	-0.76	-0.85
	TiO ₂	-	2.37	127.4	-0.47	-0.56
SrTiO ₃	AO	109.6	1.60	121.0	-0.70	-0.99
	TiO ₂	-	2.32	125.9	-0.62	-0.64
BaTiO ₃	AO	107.0	1.93	120.3	-0.70	-1.18
	TiO ₂	-	2.29	128.2	-1.05	-0.96

Table 4.3: Adsorption energies for isolated adsorption of NO and NO₂ on alkali-metal oxides. Adsorption energies are given in eV and distances in Å.

Type	O-NO(°)	O/Ti-NO	O-N-O(°)	E _{ads} (NO)	E _{ads} (NO ₂)
CaO	107.7	1.79	120.9	-0.81	-1.12
SrO	108.5	1.53	115.3	-1.15	-1.45
BaO	109.3	1.55	117.4	-1.35	-1.74

4.4 Pairwise Adsorption of NO_x on ATiO₃

Pairwise adsorption of NO_x-molecules (one NO and one NO₂) on to the ATiO₃-surfaces are performed in order to investigate possible pair-effects. Cooperative pair-effects for NO_x-adsorption has previously been reported for alkali-earth metal oxides [3][5]. The adsorption structures for BaTiO₃-surfaces are depicted in Figure 4.5. The optimal configuration is changed for the TiO₂-surface, where NO has changed its preferred binding site from Ti⁴⁺ to O²⁻. The adsorption energies of NO and NO₂ in Table 4.4 are calculated by the following equations:

$$E_{ads}(NO) = E(tot) - E(slab + NO_2) - E(NO)_g \quad (4.2)$$

$$E_{ads}(NO_2) = E(tot) - E(slab + NO) - E(NO_2)_g \quad (4.3)$$

Here, E(slab+NO_x) is the energy of a system where NO_x is adsorbed alone as described in the previous section. The total adsorption energies of NO and NO₂, E_{ads}(NO+NO₂), presented in Table 4.5, are calculated by:

$$E_{ads}(NO + NO_2) = E(tot) - E(slab) - E(NO)_g - E(NO_2)_g \quad (4.4)$$

Here, $E(\text{slab})$ is the relaxed slab energy used in 4.1. The pair effects Δ in Table 4.5 are calculated by:

$$\Delta = E_{ads}(NO + NO_2) - E_{ads}(NO_2) - E_{ads}(NO) \quad (4.5)$$

It is apparent that there are cooperative effects when NO_x molecules are adsorbed in pairs. The adsorption energies (Table 4.4) increase for both NO and NO_2 compared to the independent adsorption energies in Table 4.2, an observation that holds for all perovskite-types. Oddly, NO_x -adsorption on the TiO_2 -terminated surface has higher energy than on AO-terminated $CaTiO_3$ -surfaces. However, the total adsorption energy is still higher for the AO-terminated perovskite surface. For Ba and Sr however, pair adsorption results in higher adsorption energies for the AO-terminated surface, especially for NO_2 -adsorption. Interestingly, the most dramatic pair-effects are obtained for the $SrTiO_3$ -surfaces.

The interpretation of the adsorption energies is not completely unambiguous. A factor that might play a role is the relaxation energy. The slabs at which adsorption takes place are fixated in three out of five layers, why heavy structural relaxations are unlikely to occur. However, structural relaxations of the slab upon adsorption still occur to some extent. An example is the difference in adsorption energy when using a relaxed slab as reference and a single point calculation of the slab energy. In a single point calculation, the energy of a given structure is computed without letting the structure geometry optimize (relaxate). The difference in energy between a relaxed slab and a single point calculated slab in its adsorption structure (without adsorbates!) is 1.3 eV for an AO-terminated $BaTiO_3$ -slab (with the relaxed slab being the most energetically favorable one), which is a lot considering the small adsorption energies we are dealing with.

A comparison between adsorbate angles in Table 4.2 and Table 4.4 reveals that the pairwise adsorption results in larger angles between NO- and surface O^{2-} (O-NO) and smaller angles for NO_2 . Interestingly, the adsorption energy increases when the structure of O-NO and NO_2 approaches nitrite structure (NO_2^-), which has an angle of 115° . This can be compared to NO_x -adsorption on alkali-earth oxides, where NO_2^- formation is believed to be a precursor step to the final storage structure $Ba(NO_3)_2$ [3]. This connection between nitrite-angle and adsorption energy is not observed in the isolated adsorption processes.

4.5 Pairwise Adsorption of NO_x on AO

Adsorption energies for pairwise adsorption of NO_x on to AO-surfaces, presented in Table 4.6, shows a similar relation to O-NO and NO_2 -angles. Interesting to note is that the adsorption energies are highest for SrO, followed by BaO and CaO, results which deviates from the electropositivity trend in the case of isolated adsorption. Furthermore, the pairwise adsorption energies are of the same magnitude as for AO-terminated $ATiO_3$, but are 0.15 eV higher on SrO and 0.15 lower for the BaO compared to Sr- and Ba-perovskites.

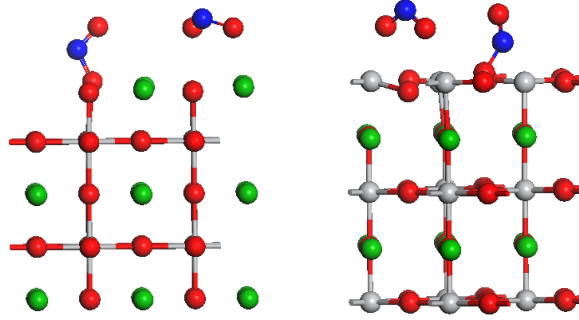


Figure 4.5: Adsorption of NO+NO₂ on AO- (left) and TiO₂-terminated (right) BaTiO₃-surface.

Table 4.4: Angles and distances between NO and surface O²⁻ and adsorption energies for pairwise adsorption of NO and NO₂ on ATiO₃-surfaces. Adsorption energies are given in eV and distances in Å.

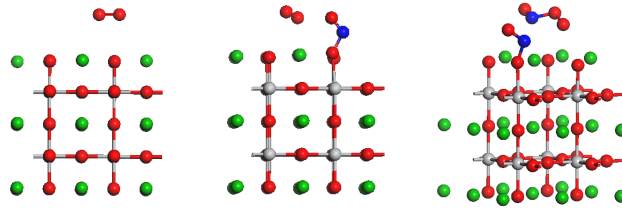
Type	Term	O-NO(°)	O/Ti-NO	NO ₂ (°)	E _{ads} (NO)	E _{ads} (NO ₂)
CaTiO ₃	AO	112.4	1.63	115.8	-1.11	-1.19
	TiO	-	1.73	118.1	-1.14	-1.23
SrTiO ₃	AO	113.7	1.38	117.2	-1.39	-1.68
	TiO	-	1.33	120.3	-1.23	-1.24
BaTiO ₃	AO	113.3	1.37	114.7	-1.31	-1.78
	TiO	-	1.36	120.9	-1.28	-1.21

Table 4.5: Total energy and pair-effects (Δ) of pairwise adsorption of NO and NO₂ on all ATiO₃-surfaces. Adsorption energies are given in eV and distances in Å.

Type	Term	E _{ads} (NO+NO ₂)	Δ
Ca	AO	-2.00	-0.34
	TiO ₂	-1.70	-0.67
Sr	AO	-2.38	-0.69
	TiO ₂	-1.87	-0.61
Ba	AO	-2.45	-0.57
	TiO ₂	-2.29	-0.28

Table 4.6: Adsorption energies for pairwise adsorption of NO and NO₂ on alkaline metal oxides. Adsorption energies are given in eV and distances in Å.

Type	O-NO(°)	O/Ti-NO	NO ₂ (°)	E _{ads} (NO)	E _{ads} (NO ₂)
CaO	111.6	1.47	117.9	-1.09	-1.40
SrO	113.3	1.38	113.9	-1.52	-1.82
BaO	111.2	1.44	116.4	-1.21	-1.59

**Figure 4.6:** The figure shows O₂, O₂ + NO and O₂ + 2NO adsorption on to BaO-terminated BaTiO₃-surface.

4.6 O₂ Influence upon Adsorption

Pairwise adsorption of O₂ and NO on a BaO-terminated perovskite-surface is studied in order to see how the presence of O₂ influence the NO adsorption energy (total adsorption energies are presented in Table 4.7). There is a cooperative effect in this case too, although not as dramatic as in the NO+NO₂-case (Table 4.5). Structure analysis shows that the O₂ bond length increase in the presence of adsorbed NO. This suggest that negative charge has been transferred to the O₂-molecule. Interestingly, this bond length increase even more when two NO-molecules are adsorbed, indicating that more negative charge has been transferred. By adding more NO-molecules on the surface, the O₂ might even dissociate to form NO₂ or NO₃⁻; a precursor structure to this dissociation can be observed in Figure 4.6.

Table 4.7: Distance between O-O and total adsorption energies and pair-effects (Δ) when O₂ is adsorbed alone and simultaneously with one or two NO-molecules.

Adsorbate	d(O-O) (Å)	E _{ads} (eV)	Δ (eV)
O ₂	1.27	-0.57	X
O ₂ +NO	1.30	-1.47	0.19
O ₂ +2NO	1.37	-2.34	0.36

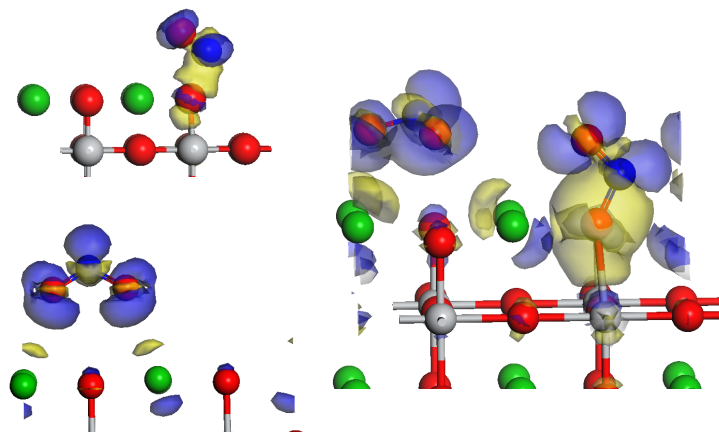


Figure 4.7: Charge density analysis for three different adsorptions on a BaO-terminated surface; NO (top left), NO₂ (bottom left) and NO+NO₂ (right). Blue and yellow areas represent accumulation and depletion of negative charge, respectively.

4.7 Electronic Structure Analysis

In order to deduce which reactions occur during the adsorption process, it is important to investigate the electron transfer between adsorbate and surface. There are several analysis methods for this within DFT. Each analysis method by itself should not be trusted blindly, but by using several, one can obtain an understanding of the electron redistribution. One simple method is to study the bond lengths and angles of the adsorbates. An increase, or decrease, of negative charge will result in altered structures. For example, the bond length of O₂ increases from 1.21 Å to 1.26 Å when the molecule becomes negatively charged (O₂⁻) [36, pp 88]. As the electron level diagram in Figure 4.2 shows, the LUMO of O₂ is an antibonding orbital, and an addition of electrons to an antibonding orbital will result in an increased repulsion between the atoms that elongates the bond. Another example is the nitrite-like structure that NO₂ approaches during pair-adsorption, suggesting that an electron has been transferred to the molecule.

An illustrative way of investigating the electron redistribution upon adsorption is to make a charge density analysis. The charge density is calculated for three systems: for the slab with molecule adsorbed on to it, for the slab alone and for the isolated adsorbate molecules. The charge densities for the isolated slab and adsorbate are then subtracted from the total (slab+adsorbate) density. The resulting difference in charge density can then be plotted together with the structure to get an illustrative picture of where the charge has been transferred. The result can be observed in Figure 4.7, which shows the charge density analysis for NO, NO₂ and NO+NO₂-adsorption on to BaO-terminated BaTiO₃. The blue and yellow colored iso-surfaces indicate that negative charge has been transferred to or from the area, respectively.

By studying the top-left picture in Figure 4.7 it is clear that the electron density redistribution for isolated NO-adsorption is a very local process. Charge is transferred *within* the adsorbate molecule rather than between surface and adsorbate. The only

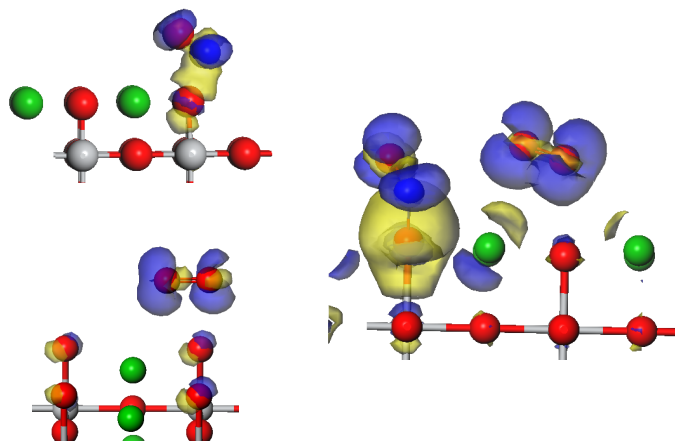


Figure 4.8: Charge density analysis for three different adsorptions on a BaO-terminated surface; NO (top left), O₂ (bottom left) and NO+O₂ (right). Blue and yellow areas represent accumulation and depletion of negative charge, respectively.

surface atom that is involved in the electron transfer process is the binding O²⁻, which can be considered part of the adsorbate molecule. As the rest of the surface stays unaffected, this reaction can be characterized as a physisorption process, an assessment supported by the rather low adsorption energies observed.

The isolated adsorption of NO₂ is a bit different as it results in a more widespread charge redistribution of surface atoms. This suggests that the adsorption in this case is a chemisorption process, as these kind of adsorption processes are characterized by a redistribution of electron density between surface and adsorbate. Previous publications of NO_x-adsorption on alkali-earth metal oxides show the same weak physisorption of NO and chemisorption behavior of NO₂ as observed here [5].

The pairwise adsorption of NO and NO₂ generates the most extensive redistribution of charge density. The areas of blue and yellow are larger, suggesting that more charge is transferred, and more widespread, suggesting that more surface atoms are involved. As previously mentioned, the adsorption energy is favored by nitrite formation between NO and surface O²⁻. However, for this to happen, NO-O²⁻ has to donate an electron. The problem is that there is no natural place for the electron to go when NO is adsorbed independently. For the nitrite formation to occur, the electron would have to go to the surface, which would occupy a state in the conduction band (above the band gap). However, the energetic penalty for this event seems to be too high, why no nitrite formation occurs during isolated NO-adsorption. When NO is adsorbed with NO₂ on the other hand, the donated electron readily finds an acceptor in NO₂, why the bond angle of both NO-O and NO₂ approaches the angle of a nitrite.

A charge density analysis is made for the NO+O₂ adsorption system as well, depicted in Figure 4.8. The pairwise adsorption is a chemisorption process. The charge density redistribution affect the surface atoms and the effect seem to affect atoms in the second layer as well. The charge transfer mechanism seems to be the same as for the NO+NO₂

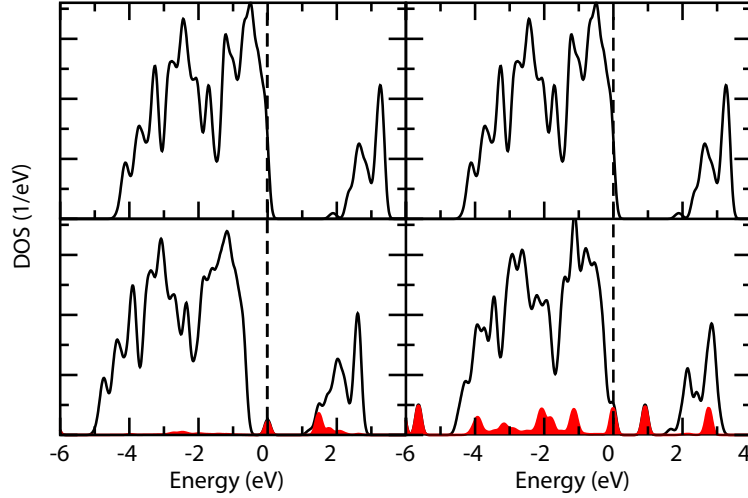


Figure 4.9: Total and projected DOS for the bare BaO-terminated BaTiO₃-slab (top), and for the same slab with NO (left) and NO+NO₂ (right) adsorbed on to it. The red fill represent states corresponding to adsorbate.

adsorption case; negative charge is transferred to the O₂-molecule from the surface O²⁻. The reason for the not so dramatic cooperative effect when NO is adsorbed with O₂ can be explained by the difference in electron affinity between the co-adsorbates O₂ and NO₂. NO₂ has an electron affinity of 2.4 eV compared to O₂ which has 0.4 eV. Due to this, NO₂ is more suitable as an electron acceptor, which explains the more dramatic increase in adsorption energy for NO when adsorbed with NO₂ compared to with O₂.

The third method used for electronic structure analysis is the before-mentioned DOS-analysis. Figure 4.9 shows a PDOS where the total DOS is projected on to the states of the adsorbate molecules (red fill). The PDOS shows that the band gap of the surface remain intact upon NO adsorption as the state in the band gap corresponds to the NO molecule. However, this is to be expected with the previous charge density discussion in mind, where NO adsorption was confirmed to be a physisorption process without electron distribution between surface and adsorbate. The pairwise chemisorption of NO and NO₂ is more interesting to study as electrons are known to redistribute. However, this process does also leave an intact surface band gap as the state in the band gap corresponds to the adsorbate.

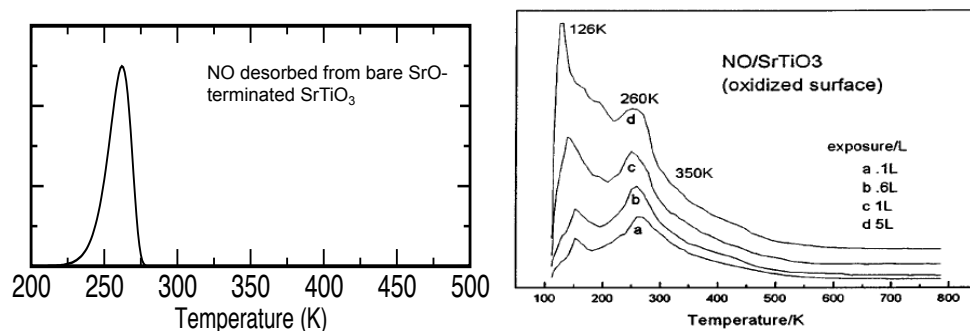


Figure 4.10: TPD-spectra of NO adsorbed on to SrO-terminated SrTiO₃ (left) compared with experiment (Rodriguez et al, Journal of Chem Phys 118, (2003)).

4.8 Calculated Experimental Observables

Results obtained from DFT-calculations should always be observed with a critical eye and not be trusted blindly. In order to verify theoretical results, reference values from experiments should be used. For this cause, experimental observables are calculated to enable comparisons between obtained results and experiments. The experimental methods described in the theory section are useful to investigate adsorption mechanisms. IR-spectra can through vibrational frequency analysis identify *what* has been adsorbed, and TPD gives information about *how strong* the interaction between adsorbate and surface is.

4.8.1 Temperature Programmed Desorption (TPD)

Looking back to the introductory chapter, the reader should be reminded that the aim is to study if the perovskite-oxides have potential to act as storing material in the combined NO_x-trap/NH₃-SCR system. In order for the material to be suited as storage material it should be able to adsorb NO_x until a certain temperature, around 150-200°C, where the NO_x should begin to desorb. The TPD-intensity shown in Figure 4.11 is calculated from the Polanyi-Wigner equation (see section 2.4.1). The pre-exponential factor A is set to 10¹³ and the heating rate (β) to 4 K/s. The initial coverage is assumed to be 1. The activation energy for desorption (E_d) is given the value of the adsorption energy. Both A and E_d are assumed to be coverage independent. Desorption temperatures have been calculated for NO_x on AO-terminated and TiO₂-terminated perovskites (Table 4.8 and Table 4.9, respectively.)

Published results from TPD experiments made on SrTiO₃-surfaces show desorption peaks at 260 K [37], which agrees well with the calculated value of 250 K for Sr (Figure 4.10). However, the desorption temperature is too low to be applicable for the NO_x-trap. The TPD-curve for NO adsorbed in pair with NO₂ shows better promise, with desorption temperature at around 200°C for BaO-terminated perovskite-surfaces.

Table 4.8: Temperature of desorption for isolated NO and for pair adsorbed NO_x on AO-terminated perovskite-surfaces. The desorption temperatures are estimated from a graph. The energies are given in eV and the temperature in K.

Perovskite	Ads	E_{ads}	T_{des}	Ads	E_{ads}	T_{des}
CaTiO ₃	NO	-0.76	275	NO ₂	-0.85	310
	NO/NO ₂	-1.11	400	NO ₂ /NO	-1.19	440
SrTiO ₃	NO	-0.70	250	NO ₂	-0.99	350
	NO/NO ₂	-1.39	500	NO ₂ /NO	-1.68	600
BaTiO ₃	NO	-0.70	250	NO ₂	-1.18	410
	NO/NO ₂	-1.31	470	NO ₂ /NO	-1.77	630

Table 4.9: Temperature of desorption for isolated NO and for pair adsorbed NO_x on TiO₂-terminated perovskite-surfaces. The desorption temperatures are estimated from a graph. The energies are given in eV and the temperature in K

Perovskite	Ads	E_{ads}	T_{des}	Ads	E_{ads}	T_{des}
CaTiO ₃	NO	-0.47	170	NO ₂	-0.56	205
	NO/NO ₂	-1.14	410	NO ₂ /NO	-1.23	450
SrTiO ₃	NO	-0.62	225	NO ₂	-0.64	220
	NO/NO ₂	-1.23	440	NO ₂ /NO	-1.24	450
BaTiO ₃	NO	-1.05	380	NO ₂	-0.96	340
	NO/NO ₂	-1.33	480	NO ₂ /NO	-1.24	450

4.8.2 Vibrational Analysis

The vibrational frequencies of pair adsorbed NO and NO₂ on AO- and TiO₂-terminated BaTiO₃ surfaces are calculated. The calculation is done on an optimized structure, allowing the six atoms (NO₂ and bonding surface+NO, denoted O-NO) to vibrate. The calculated frequencies are presented in Table 4.10.

The vibrational frequencies for gas-phase NO and NO₂, discussed in Section 4.1, are 1893 cm⁻¹ for NO and 741, 1338 and 1641 cm⁻¹ for NO₂. As electron structure analysis indicate that pair-adsorbed NO and NO₂ form nitrite structure, vibrational frequencies are calculated for gas phase NO₂⁻ as well, giving values of 761, 1189 and 1290 cm⁻¹. A comparison between these values and the results in Table 4.10 suggests that the adsorbed NO₂-molecule has formed nitrite structure. The frequencies of NO₂ on AO-terminated perovskites agree better with the nitrite gas phase frequencies than NO₂ adsorbed on

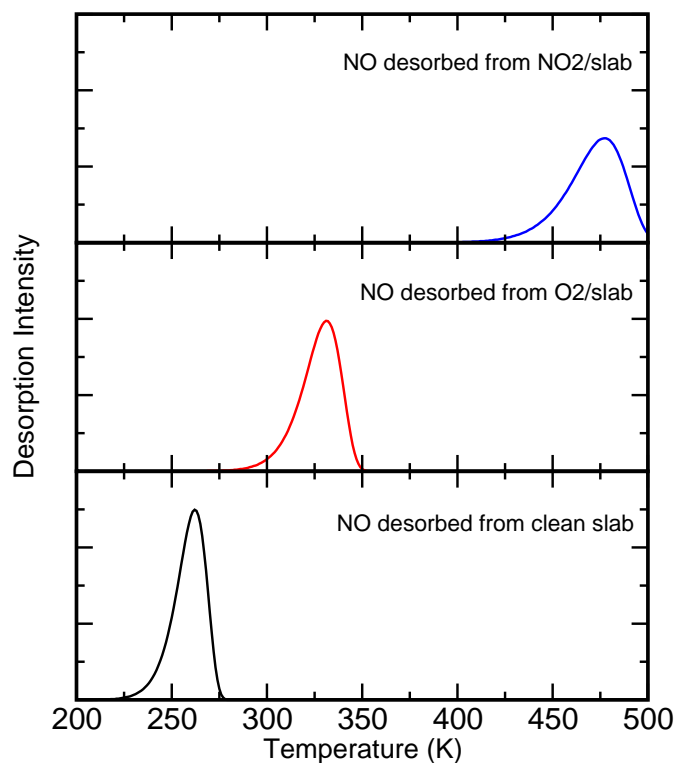


Figure 4.11: Desorption temperatures for NO when adsorbed isolated (bottom), simultaneous with O₂ (middle) and NO₂ (top) on a BaO-terminated BaTiO₃ surface.

Table 4.10: Vibrational frequencies for pairwise adsorption of NO and NO₂ on AO- and TiO₂-terminated BaTiO₃-surfaces.

Molecule	Mode	Vib(cm ⁻¹)	
		AO	TiO ₂
O-NO	sym	1443	1671
O-NO	asym	867	915
O-NO	bend	712	704
NO ₂	sym	1236	1200
NO ₂	asym	1207	1139
NO ₂	bend	775	737

TiO₂-terminated surfaces. This complies well with the results in Table 4.4, showing that the NO₂-angles are closer to 115° when NO₂ is pair-adsorbed on AO-surfaces compared to TiO₂-surfaces.

The results are not as clear for O-NO. The symmetric stretching mode has a much higher frequency than the other two modes. Atomic weights and vibrational simulations show that this vibration corresponds to the stretching mode of NO rather than of NO₂. The results here suggest that O-NO has not formed a real nitrite.

5

Discussion and Conclusions

As previously stated, a combined NO_x -trap and NH_3 -SCR catalysis is a promising solution to control NO_x emissions in lean burn engines. The idea behind the method is to trap NO_x in a storage material at low temperatures, and then release and reduce it by ammonia at temperatures around 150-200 °C. Here, adsorption of NO_x on perovskites have been studied within the Density Functional Theory, to investigate the compound's capability of storing NO_x at desired temperatures. Comparisons are made with adsorption on alkali-earth metal oxide surfaces, as BaO is the current storage material for industry NSR-catalysis. These objectives are repeated to remind the reader about the scope of the project. The most important findings of the project are briefly discussed below.

The CaTiO_3 perovskite is not stable in its cubic structure and undergoes orthorhombic distortions. Ba - and SrTiO_3 on the other hand, seem stable in their cubic structures.

The AO-terminated surface is the more stable one for CaTiO_3 -perovskites, whereas the TiO_2 -terminated surface is slightly more stable for Ba and Sr. However, the energetic difference is very small, why both terminations are expected to be present in experiments.

The adsorption energy does not seem to depend on the A-ion for NO adsorption on perovskite-surfaces. For NO adsorbed on alkali-metal oxides however, the adsorption energy is strictly dependent on the electropositivity of A. NO interacts stronger with AO-surfaces than with perovskite-surfaces.

Charge density analysis and adsorption energies indicate that NO physisorbs on to perovskite-surfaces. The desorption temperature is around 250 K for AO-terminated Ba and Sr-perovskite surfaces, which is too low for the NO_x -trap application. The calculated desorption temperatures agrees well with experimental results. However, the

Table 5.1: Comparison of pair-effects between pairwise adsorption of NO/NO₂ and NO/O₂ on BaO-terminated BaTiO₃. The energy is given in eV.

Adsorbate	O-NO (°)	O-NO (Å)	E _{ads} (NO)
NO	107.0	1.93	0.70
NO + O ₂	111.9	1.43	0.90
NO + NO ₂	113.3	1.37	1.31

experiments were performed at very low temperatures (NO was adsorbed at 100 K). Adsorption performed at higher temperatures (in the presence of oxygen) might very well result in that NO is stored as something else, possibly NO₂⁻ or NO₃⁻, which would generate higher desorption temperatures.

NO₂ chemisorbs on to perovskite surfaces and the adsorption energy increase with the electropositivity of A, according to the sequence Ba > Sr > Ca. This trend holds for adsorption on both perovskite terminations and alkali-earth oxide-surfaces. The adsorption energy is higher for NO₂ adsorption than for NO adsorption.

There are significant pair-effects when NO is adsorbed with NO₂. This holds for adsorption on all perovskite-surfaces and alkali-earth metal oxides. Interesting to note is that the pair-effects are most dramatic for Sr, for both perovskite- and AO-surfaces. As the interaction between adsorbate and surface increases upon pair-adsorption, so does the desorption temperature, which is elevated to the desired temperature for the NO_x-trap application.

The energy of pairwise adsorption of NO and NO₂ depends on the formed bond angle between O-NO and NO₂. The adsorption energy increase when the angles approach the angle of a nitrite. Charge density analysis show that negative charge is transferred from the binding surface O²⁻ to the NO₂-molecule, making both molecules approach nitrite structure. However, vibrational analysis shows that NO₂ shows greater resemblance with a nitrite than O-NO, an assessment that can be confirmed by structure analysis. The bond angle of O-NO is 113.3° and the angle of NO₂ is 114.7° for pair-adsorption on AO-terminated BaTiO₃ (Table 4.4), to be compared with the gas-phase nitrite which has a bond angle of 115.16. Also, the bond length within the molecule is not symmetric. The distances between O-N-O is 1.37 Å and 1.28 Å, compared to the nitrite gas-phase bond length of 1.283 Å.

Cooperative pair-effects occur when NO is adsorbed in pair with O₂ as well. The mechanism seem to be the same; an electron is transferred from the surface O²⁻ and picked up by the O₂-molecule. Table 5.1 shows that the adsorption energy for pair-adsorption depends on the O-NO angle, as the energy increases when nitrite structure

is approached. Pair adsorption of NO and O₂ results in an elongated bond length of O₂. The bond length is further ielongated when multiple NO are adsorbed, suggesting that O₂ will eventually dissociate to form NO₂⁻ or NO₃⁻ with NO and surface O²⁻.

Outlook

To further investigate perovskite-oxides as storage material it would be fruitful to compare the calculated vibrational frequencies with experimental results. An IR-spectroscopy on perovskite-oxides powders after NO_x-adsorption would possibly reveal in what form NO_x is adsorbed.

On the computational side, it would be of interest to investigate the coverage dependence of the adsorption energy, and how the distance between pair-adsorbed NO_x-molecules affect the adsorption energy. Furthermore, it would be interesting to dope the perovskite surfaces with mixed A-ions to see how narrow the desorption temperature can be adjusted. Also, it would be interesting to alter the B-ion to see how this affect adsorption energies. As physical surface experiments suggest that perovskite surfaces reconstruct to some extent, it would be of interest to run calculations on reconstructed surfaces to enable comparisons with surface experiments.

Bibliography

- [1] S. Tamm, S. Andonova, L. Olsson, Silver as storage compound for nox at low temperatures, *Catalysis Letters* 144 (2014) 674–684.
- [2] F. Can, X. Courtois, S. Royer, G. Blanchard, S. Rousseau, D. Duprez, An overview of the production and use of ammonia in nsr+scr coupled system for nox reduction from lean exhaust gas, *Catalysis Today* 197 (2012) 144–154.
- [3] H. Grönbeck, P. Broqvist, I. Panas, Fundamental aspects of nox adsorption on bao, *Surface Science* 600 (2006) 403–408.
- [4] T. Johnson, Vehicular emissions in review, *SAE Int. J. Engines*.
- [5] W. Schneider, K. Hass, M. Miletic, J. Gland, Dramatic cooperative effects in adsorption of nox on mgo(001), *The Journal of Physical Chemistry B* 106 (30) (2002) 7405–7413.
- [6] J. Bednorz, K. Müller, Perovskite-type oxides - the new approach to high-*t_c* superconductivity, *Angewandte Chemie* 100 (5) (1988) 757.
- [7] L. Tejuca, J. Fierro, Structure and reactivity of perovskite-type oxides, *Advances in Catalysis* 36 (1989) 237–328.
- [8] C. Cramer, *Essentials of Computational Chemistry Theories and Models*, 2nd Edition, John Wiley & Sons, 2004.
- [9] P. Atkins, J. Paula, R. Friedman, *Quanta, Matter and Change - A molecular approach to physical chemistry*, Oxford University Press, 2009.
- [10] W. Koch, M. Holthausen, *A Chemist’s Guide to Density Functional Theory*, 2nd Edition, Wiley-VCH, 2001.
- [11] F. Jensen, *Introduction to computational chemistry*, 2nd Edition, John Wiley & Sons, 2007.

- [12] K. Burke, Perspective of density functional theory, *The Journal of Chemical Physics* 136.
- [13] P. Hohenberg, W. Kohn, Inhomogeneous electron gas, *Physical Review* 136 (3B).
- [14] W. Kohn, L. Sham, Self-consistent equations including exchange and correlation effects, *Physical Review* 140 (4A).
- [15] K. Burke, L. Wagner, Dft in a nutshell, *International Journal of Quantum Chemistry* 113 (2013) 96–101.
- [16] R. Martin, *Electronic Structure - Basic Theory and Practical Methods*, Cambridge University Press, 2004.
- [17] B. Delley, An all-electron numerical method for solving the local density functional for polyatomic molecules, *The Journal of Chemical Physics* 92 (1990) 508–517.
- [18] H. Grönbeck, First principles studies of metal-oxide surfaces, *Topics in Catalysis* 28.
- [19] J. Perdew, K. Burke, M. Ernzerhof, Generalized gradient approximation made simple, *Physical Review Letters* 77 (18) (1996) 3865–3868.
- [20] P. Atkins, L. Jones, *Chemical Principles, The Quest for Insight*, forth Edition, W.H Freeman and Company, 2008.
- [21] I. Chorkendorff, J. Niemantsverdriet, *Concepts of Modern Catalysis and Kinetics*, Wiley-VCH, 2003.
- [22] D. McQuarrie, J. Simon, *Molecular Thermodynamics*, University Science Books, 1999.
- [23] P. Broqvist, H. Grönbeck, I. Panas, Surface properties of alkaline earth metal oxides, *Surface Science* 554 (2004) 262–271.
- [24] Z. Zeng, F. Calle-Vallejo, M. Mogensen, J. Rossmeisl, Generalized trends in the formation energies of perovskite oxides, *Physical Chemistry, Chemical Physics* 15 (2013) 7526–7533.
- [25] A. Verma, V. Jindal, Lattice constant of cubic perovskites, *Journal of Alloys and Compounds* 485 (2009) 514–518.
- [26] A. Verma, A. Kumar, Bulk modulus of cubic perovskites, *Journal of Alloys and Compounds* 541 (2012) 210–214.
- [27] R. Hoffman, A chemical and theoretical way to look at bonding on surfaces, *Reviews of Modern Physics* 60 (3) (1988) 601–623.

-
- [28] P. Cortona, A. Monteleone, Ab initio calculations of cohesive and structural properties of the alkali-earth oxides, *Journal of Physics: Condensed Matter* 8 (1996) 8983–8994.
- [29] E. Cockayne, B. Burton, Phonons and static dielectric constant in CaTiO_3 from first principles, *Physical Review B* 62 (6).
- [30] S. Piskunov, E. Kotomin, E. Heifets, J. Maier, R. Eglitis, G. Borstel, Hybrid dft calculations of the atomic and electronic structure for ABO_3 perovskite (0 0 1) surfaces, *Surface Science* 575 (2005) 75–88.
- [31] J. Padilla, D. Vanderbilt, Ab initio of BaTiO_3 surfaces, *Physical Review B* 56 (3) (1997) 1625–1631.
- [32] E. Heifets, R. Eglitis, E. Kotomin, J. Maier, G. Borstel, Ab initio modeling for surface structure for SrTiO_3 perovskite crystals, *Physical Review B* 64.
- [33] K. Huber, G. Herzberg, *Molecular Spectra and Molecular Structure IV. Constants of diatomic molecules*, Van Nostrand Reinhold Company, 1979.
- [34] L. Sutton (Ed.), *Tables of Interatomic Distances and Configuration in Molecules and Ions*, 18th Edition, London: The chemical Society, 1965.
- [35] H. Hodjati, K. Vaezzadeh, C. Petit, V. Pitchon, A. Klennemann, Adsorption/desorption of NO_x process on perovskites: performances to remove NO_x from a lean exhaust gas, *Applied Catalysis B* 26 (2000) 5–16.
- [36] H. Gray, *Chemical Bonds: An Introduction to Atomic and Molecular Structure*, University Science Books, 1994.
- [37] J. Rodriguez, S. Azad, L. Wang, J. Garcia, A. Etxebarria, L. Gonzalez, Electronic and chemical properties of mixed-metal oxides: Adsorption and reaction of NO on SrTiO_3 (100), *The Journal of Chemical Physics* 118 (14) (2003) 6562–6571.